

NEDO-30130-A  
CLASS I  
MAY 1985

LICENSING TOPICAL REPORT

# STEADY-STATE NUCLEAR METHODS

8507260500 850723  
PDR TOPRP EMVGENE  
C PDR

GENERAL  ELECTRIC

NEDO-30130-A  
Class I  
May 1985

LICENSING TOPICAL REPORT

STEADY-STATE NUCLEAR METHODS

---

NUCLEAR POWER SYSTEMS DIVISION • GENERAL ELECTRIC COMPANY  
SAN JOSE, CALIFORNIA 95125

---

**GENERAL**  **ELECTRIC**

**DISCLAIMER OF RESPONSIBILITY**

*This document was prepared by or for the General Electric Company. Neither the General Electric Company nor any of the contributors to this document:*

- A. Makes any warranty or representation, express or implied, with respect to the accuracy, completeness, or usefulness of the information contained in this document, or that the use of any information disclosed in this document may not infringe privately owned rights; or*
- B. Assumes any responsibility for liability or damage of any kind which may result from the use of any information disclosed in this document.*

t



UNITED STATES  
NUCLEAR REGULATORY COMMISSION  
WASHINGTON, D. C. 20555

DEC 22 1983

Ms. J. S. Charnley  
Fuel Licensing Manager  
Nuclear Safety & Licensing Operation  
General Electric Company  
175 Curtner Avenue  
San Jose, California 95125

Dear Ms. Charnley:

Subject: Acceptance for Referencing of Licensing Topical Report  
NEDE-30130, "Steady-State Nuclear Methods"

We have completed our review of the subject topical report submitted July 21, 1983, by General Electric Company (GE). We find this report is acceptable for referencing in license applications to the extent specified and under the limitations delineated in the report and the associated NRC evaluation which is enclosed. The evaluation defines the basis for acceptance of the report.

We do not intend to repeat our review of the matters described in the report and found acceptable when the report appears as a reference in license applications except to assure that the material presented is applicable to the specific plant involved. Our acceptance applies only to the matters described in the report.

In accordance with procedures established in NUREG-0390, it is requested that GE publish accepted versions of this report, proprietary and non-proprietary, within three months of receipt of this letter. The accepted versions should incorporate this letter and the enclosed evaluation between the title page and the abstract. The accepted versions shall include an -A (designating accepted) following the report identification symbol.

Should our criteria or regulations change such that our conclusions as to the acceptability of the report are invalidated, GE and/or the applicants referencing the topical report will be expected to revise and resubmit their respective documentation, or submit justification for the continued effective applicability of the topical report without revision of their respective documentation.

Sincerely,

*Dino C. Scoleto*  
for Cecil O. Thomas, Chief  
Standardization & Special  
Projects Branch  
Division of Licensing

Enclosure: As stated



EVALUATION OF A  
GENERAL ELECTRIC LICENSING TOPICAL REPORT

Report Number: NEDE-30130 (Proprietary)  
Report Title: Steady-State Nuclear Methods  
Report Date: June 1983  
Originating Organization: General Electric Company  
Reviewed By: Daniel Fieno, Core Performance Branch/DSI

The General Electric Company (GE) has submitted Licensing Topical Report NEDE-30130 entitled "Steady-State Nuclear Methods" for our review. This report provides a description of improved GE methods for core modeling and fuel assembly modeling. Our evaluation of this report follows.

#### 1. SUMMARY OF REPORT

The purpose of the report is to describe the methods and data used by GE to model the heterogeneous boiling water reactor (BWR) core. The report consists of four main sections: (1) a section on the three-dimensional nuclear model, (2) a section on lattice physics methods, (3) a section on the thermal-hydraulic model, and (4) a section on model qualification.

The section on the three-dimensional nuclear model discusses the PANACEA BWR core simulator code. PANACEA is a three-dimensional, coupled nuclear and thermal-hydraulic, time independent model of the BWR core exclusive of any external flow loops. PANACEA is used for three-dimensional design and operational calculations of BWR power distributions and thermal performance as a function of control rod position, fuel loading pattern, coolant flow, reactor pressure, and other operational and design variables. The program is capable of performing fuel cycle and thermal limits calculations. A special power and exposure iteration option is available for target exposure distributions and cycle length determinations.

The section on lattice physics methods discusses the TGBLA code. The report discusses the generation of few group neutron cross section by means of the neutron spectra calculations, the calculation of fuel rod power distributions for a fuel bundle, and the evaluation of the effects of fuel exposure. The output of TGBLA is used as input to PANACEA.

The section on the thermal-hydraulic model discusses the void-quality correlation, the bypass region calculation, the total core energy balance, and the thermal limits calculations. The thermal-hydraulic model is coupled to the neutronics model of PANACEA. Iterations are performed on power and flow until a consistent solution is obtained by PANACEA for this neutronic and thermal-hydraulic coupling.

Model qualification is presented in the last major section of the report. Extensive operating plant tracking results are presented. Comparisons of calculations are presented for gamma scan measurements taken at the end of six operating fuel cycles. Results are also presented on comparisons of cold critical measurements taken at two plants over seven cycles of operation.

This report presents the improvements made in the GE nuclear design methods. Additional information on these methods can be found in the previously reviewed and approved GE licensing topical reports. These reports are:

1. NEDE-20913-P-A, "Lattice Physics Methods," February 1977.
2. NEDO-20939-A, "Lattice Physics Methods Verification," January 1977.
3. NEDO-20953-A, "Three-Dimensional Core Simulator," January 1977.
4. NEDO-20946-A, "Simulator Methods Verification," January 1977.
5. NEDO-20964, "Void and Doppler Reactivity Feedback," December 1975.

## 2. SUMMARY OF EVALUATION

Our evaluation is based, in part, on the information provided by GE in the topical report. In addition, we had a meeting with GE on May 26, 1983 to discuss the GE improved nuclear design methods (see meeting summary by D. B. Fieno to C. H. Berlinger entitled "Summary of Meeting with GE on Improvements to Reactor Physics Methods," dated May 31, 1983). We performed the review of the five GE licensing topical reports listed above. We also participated in the extensive staff evaluation of the ODYN transient model described in NEDO-24154 and NEDE-24154-P, Volumes I, II and III. Our review involved the neutronic methods incorporated in ODYN. The approval letter transmitting the staff evaluation of the ODYN transient model was sent on February 4, 1981 from R. Tedesco (NRC) to G. Sherwood (GE). Our evaluation is based, therefore, on the submitted report and on our extensive previous review efforts on GE nuclear design methods.

### BWR Core Simulator (PANACEA)

We have reviewed the three-dimensional neutronics model used in the PANACEA code. The model is based on a coarse mesh nodal approximation to the neutron steady-state diffusion equation. One energy group is used in this model to represent fast energy neutron diffusion. Resonance energy and thermal energy neutronic effects are included in the model by relating the resonance and thermal energy fluxes to the fast energy flux. Neutronic parameters used by PANACEA are obtained from TGBLA and parametrically fitted as a function of moderator density, exposure, control and moderator density history for a given fuel type.

PANACEA includes the effect of Doppler broadening as a function of effective average fuel temperature, the effect of equilibrium xenon, and the effect of crud buildup on the cladding. The equations describing the treatment of these effects are presented. The conversion of flux to power and the evaluation of travelling incore monitor (TIP) response are also presented.

We have reviewed the assumptions inherent in the PANACEA model, the derivation of the equations used, the evaluation of special reactivity effects, and the representation of fast, resonance, and thermal energy effects. We conclude that the PANACEA model is state-of-the-art and representative of its class of nodal methods and is, therefore, acceptable.

#### Lattice Physics Methods (TGBLA)

We have reviewed the neutronics models of the TGBLA code. The primary purpose of these modules is to account for the fine structure of the BWR lattice in generating nuclear data for use by PANACEA. The mathematical details of the spectra calculations in the fast, resonance and thermal energy ranges have been reviewed. We have reviewed the assumptions in the models, the improvements made to previous models, and the derivation of the equations. The cross sections used are based primarily on ENDF-BV. We conclude that TGBLA along with its input data base is a state-of-the-art lattice physics model and is, therefore, acceptable.

#### Thermal-Hydraulics Model

The power-void feedback interaction has an important effect on the nuclear calculations. The report describes the thermal-hydraulic model used in PANACEA. The model is similar to that previously used in GE nuclear design models. Improvements have been made to the void-quality correlation. We have reviewed the changes in the thermal-hydraulic model to that previously reviewed and approved for use in the BWR core simulator code. We conclude that the thermal-hydraulic model is typical of the type used for BWR nodal codes, that is, state-of-the-art, and, therefore, is acceptable.

#### Model Qualification

We have discussed our review of the assumptions and equations of the GE nuclear design methods. We have found them to be state-of-the-art and, therefore, acceptable. No matter how well-founded the mathematical models may be, model qualification provides the final step in assessing

the usefulness and accuracy of the nuclear design methods. This GE nuclear design model has undergone extensive testing by comparison of calculated results with operating reactor data, end-of-cycle gamma scan data, and critical configurations.

Hot critical effective multiplication factors ( $k_{eff}$ ) have been tracked for a number of plants at different exposure points and for different operating cycles. The average calculated  $k_{eff}$  is 1.002 with an RMS of 0.002. The data do not indicate any significant bias with exposure. The results indicate that the GE nuclear design models track core reactivity very well and compare well with results reported by others.

Numerous examples of the ability of the GE nuclear design models to track the core power distributions are given. The results are shown for the core average axial power distributions for a number of plants at various exposure points and operating cycles. The calculated results show that the GE methods track the measured (by the process computer) core average axial power distributions very well.

A further indication of the GE nuclear design methods ability to track operating plants is the comparison of calculated results with gamma scan measurements. The results are given for the lanthanum-140 gamma activity which comes from the beta decay of barium-140. This lanthanum activity follows the actual power distribution and is indicative of the power distribution prior to reactor shutdown for end-of-cycle. Gamma scan measurements were taken at the end of six cycles of three operating reactors (Hatch Unit 1, Quad Cities Unit 1 and Millstone Unit 1). The results presented for the gamma scans show that the calculations agree very well with the measured data for the interior bundles. Peripheral bundle locations show larger deviations. The nodal comparison has an RMS between 4 percent and 6 percent and the integrated bundle comparison RMS is between 2 and 3 percent for the six measured cycles of operation.

Cold critical effective multiplication factors have been calculated and compared to a number of measured points. The average cold calculated  $k_{eff}$  is 0.9986 with an RMS of 0.0033. These results indicate that the GE nuclear design methods track the cold  $k_{eff}$  very well.

The results presented in the report clearly show that the improvements made to the GE nuclear design model yield improved accuracy for the model.

### 3. EVALUATION PROCEDURE

The review of licensing topical report NEDE-30130 has been conducted within the guidelines provided by Section 4.3 of the Standard Review Plan. Sufficient information has been provided to permit the conclusion that the improved GE nuclear design methods are state-of-the-art and are, therefore, acceptable.

### 4. REGULATORY POSITION

Based on our review of licensing topical report NEDE-30130 we conclude that it is acceptable for reference by GE in licensing submittals.

## CONTENTS

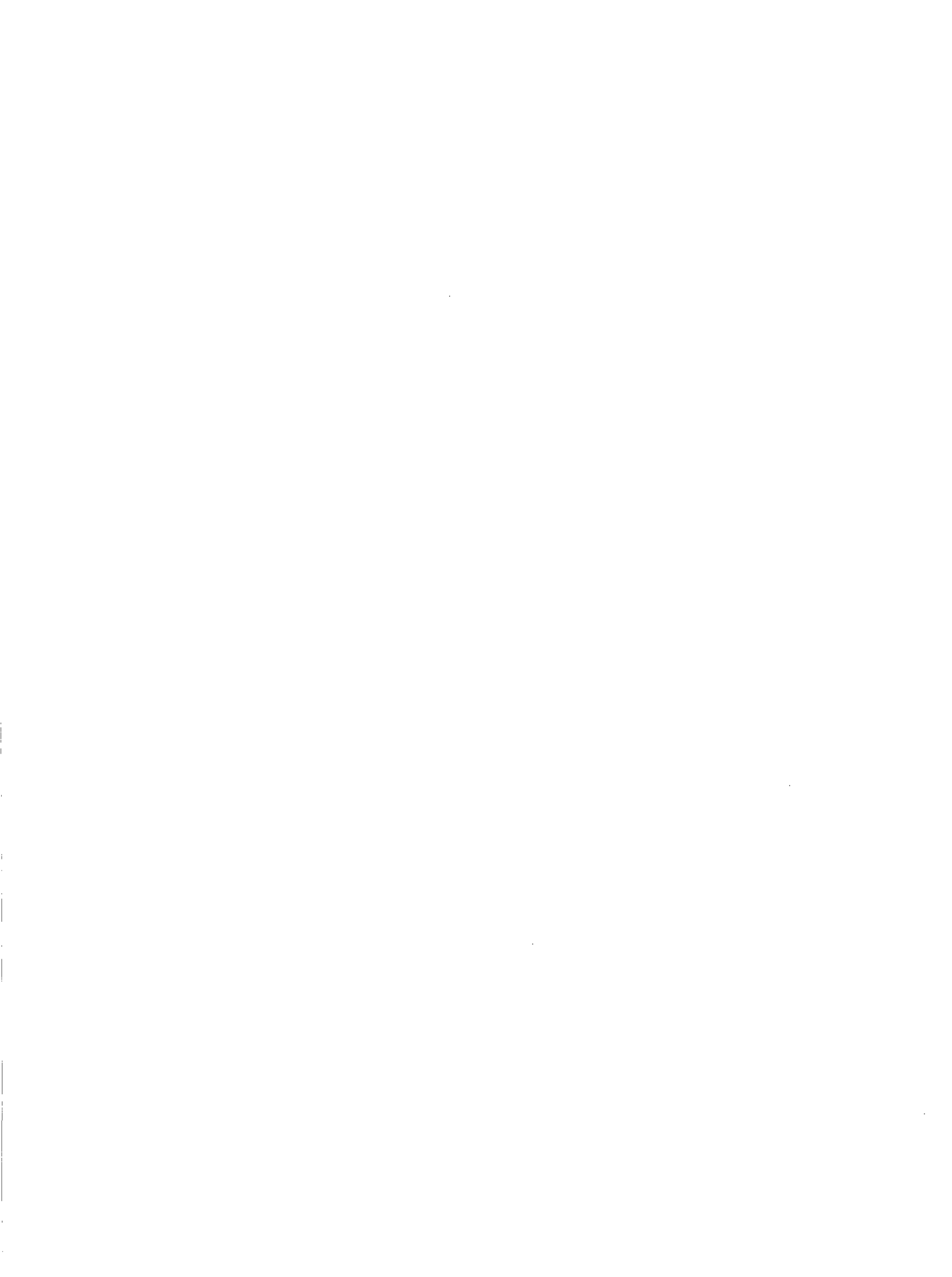
	<u>Page</u>
ABSTRACT	xvii
ACKNOWLEDGMENTS	xviii
1. INTRODUCTION	1-1
2. THREE-DIMENSIONAL NUCLEAR MODEL	2-1
2.1 Coarse Nodal, One-Group Diffusion Theory	2-2
2.2 Void and Exposure Effects	2-6
2.3 Control Rod Effects	2-7
2.4 Doppler Effects	2-8
2.5 Xenon Effects	2-8
2.6 Crud Effects	2-10
2.7 Conversion of Flux to Power	2-11
2.8 Isotopic Tracking	2-12
2.9 Traveling In-Core Probe (TIP) Calculation	2-12
2.10 Power-Void Iteration	2-14
2.11 Halting Power-Exposure Iteration	2-16
2.12 References	2-16
3. DETAILED LATTICE PHYSICS METHODS	3-1
3.1 General Description of Solution Techniques	3-1
3.2 Thermal Neutron Spectrum and Diffusion Parameter Calculations	3-3
3.2.1 Thermal Library Condensation	3-4
3.2.2 Thermal Neutron Spectrum Calculation	3-4
3.2.3 Thermal Homogenized Cross Section and Diffusion Coefficient Generation	3-9
3.2.4 $P_1$ Blackness Theory	3-10
3.3 Fast and Epithermal Spectrum and Diffusion Parameter Calculations	3-10
3.3.1 Dancoff Factor Calculation	3-10
3.3.2 Resolved Resonance Range Approximation	3-11
3.3.3 Unresolved Resonance Treatment	3-11
3.3.4 Determination of Heterogeneity Correction Factors From Averaged Fuel Rod - Cell Transport Calculation	3-13
3.3.5 Fine-Group Transport Calculation for One-Dimensional Equivalent Bundle	3-13
3.4 Bundle Flux, Power and Miscellaneous Calculations	3-14
3.4.1 Two-Dimensional Few-Group Coarse-Mesh Diffusion Calculation	3-14
3.4.2 Power-Related Distributions	3-16
3.4.3 Bundle-Average Diffusion Parameters	3-19

## CONTENTS (Continued)

	<u>Page</u>
3.5 Nuclide Depletion Calculation	3-19
3.5.1 Fission-Related Nuclide Chains	3-20
3.5.2 Nuclide Depletion in Fuel Rods	3-20
3.6 References	3-24
4. THERMAL-HYDRAULICS MODEL	4-1
4.1 Flow Distribution	4-2
4.2 Enthalpy-Quality Distribution Calculation	4-9
4.3 Void-Quality Correlation	4-11
4.4 Bypass Region Calculation	4-12
4.5 Total Core Energy Balance	4-13
4.6 Thermal Limits Calculation	4-14
4.7 References	4-16
5. MODEL QUALIFICATION	5-1
5.1 Introduction	5-1
5.2 Plant Tracking Results	5-1
5.2 Gamma Scan Comparisons	5-17
5.3 Cold Critical Measurements	5-27
5.4 Isotopic Burnup Verification	5-27
5.5 References	5-50
APPENDIX A	A-1

## TABLES

<u>Table</u>	<u>Title</u>	<u>Page</u>
3-1	Group Structure of 16-Group Thermal Library	3-5
5-1	Summary of Hot Critical $k_{eff}$	5-2
5-2	Nodal and Bundle Integrated Power Comparisons Gamma Scan vs. Calculation	5-18
5-3	Quad Cities Cold Critical Eigenvalues	5-29



## ILLUSTRATIONS

<u>Figure</u>	<u>Title</u>	<u>Page</u>
2-1	Power-Void Iteration Flow Chart	2-15
2-2	Power-Exposure Iteration Flow Chart	2-17
3-1	Bundle Configuration	3-2
3-2	An Equivalent Fuel Cell	3-6
3-3	Various Dancoff Pairs in the BWR Lattice	3-12
3-4	Typical Mesh Point and Its Nearest Neighbors	3-16
3-5	Fissionable Nuclide Chains	3-21
4-1	Schematic of Characteristic Channel Nodalization	4-4
4-2	Flow Channel Geometry	4-10
5-1	Hatch 1 Cycle 1: $k_{eff}$ Versus Exposure	5-3
5-2	Hatch 1 Cycle 2: $k_{eff}$ Versus Exposure	5-3
5-3	Hatch 1 Cycle 3: $k_{eff}$ Versus Exposure	5-4
5-4	Quad Cities 1 Cycle 1: $k_{eff}$ Versus Exposure	5-4
5-5	Quad Cities 1 Cycle 2: $k_{eff}$ Versus Exposure	5-5
5-6	Quad Cities 1 Cycle 3: $k_{eff}$ Versus Exposure	5-5
5-7	Quad Cities 1 Cycle 4: $k_{eff}$ Versus Exposure	5-6
5-8	Quad Cities 1 Cycle 5: $k_{eff}$ Versus Exposure	5-6
5-9	Millstone Cycle 7: $k_{eff}$ Versus Exposure	5-7
5-10	Hatch 1 Cycle 1: Core Average Axial Power	5-8
5-11	Hatch 1 Cycle 2: Core Average Axial Power	5-9
5-12	Hatch 1 Cycle 3: Core Average Axial Power	5-10
5-13	Quad Cities 1 Cycle 1: Core Average Axial Power	5-11

## ILLUSTRATIONS (Continued)

<u>Figure</u>	<u>Title</u>	<u>Page</u>
5-14	Quad Cities 1 Cycle 2: Core Average Axial Power	5-12
5-15	Quad Cities 1 Cycle 3: Core Average Axial Power	5-13
5-16	Quad Cities 1 Cycle 4: Core Average Axial Power	5-14
5-17	Quad Cities 1 Cycle 5: Core Average Axial Power	5-15
5-18	Millstone 1 Cycle 7: Core Average Axial Power	5-16
5-19	Hatch 1, Cycle 1: Axial Barium Distribution	5-19
5-20	Hatch 1, Cycle 3: Axial Barium Distribution Axial Distribution	5-19
5-21	Quad Cities 1, Cycle 2: Axial Barium Distribution	5-19
5-22	Quad Cities 1, Cycle 4: Axial Barium Distribution	5-19
5-23	Quad Cities, Cycle 5: Axial Barium Distribution	5-20
5-24	Millstone, Cycle 7: Axial Barium Distribution	5-20
5-25	Hatch 1, End of Cycle 1: Bundle Power Comparisons	5-21
5-26	Hatch 1, End of Cycle 3: Bundle Power Comparisons	5-22
5-27	Quad Cities 1, End of Cycle 2: Bundle Power Comparisons	5-23
5-28	Quad Cities 1, End of Cycle 4: Bundle Power Comparisons	5-24
5-29	Quad Cities 1, End of Cycle 5: Bundle Power Comparisons	5-25
5-30	Millstone End of Cycle 7: Bundle Power Comparisons	5-26

## ABSTRACT

The improved General Electric methods for coarse-mesh core modeling (BWR Core Simulator) and for bundle modeling (lattice physics methods) are described.

The BWR Core Simulator is a static, three-dimensional coupled nuclear-thermal-hydraulic computer program representing the BWR core exclusive of the external flow loop. Provisions are made for fuel cycle and thermal limits calculations. The program is used for detailed three-dimensional design and operational calculations of BWR neutron flux and power distributions and thermal performance as a function of control rod position, refueling pattern, coolant flow, reactor pressure, and other operational and design variables. A special power-exposure iteration option is available for target exposure distribution and cycle length predictions. The nuclear model is based on coarse-mesh nodal, one-group, static diffusion theory. Eigenvalue iteration yields the fundamental mode solution. This is coupled to static parallel channel thermal-hydraulics containing a modified Zuber-Findlay void-quality correlation. Pressure drop balancing yields the flow distribution.

Lattice physics calculations are performed using a two-dimensional, fine mesh, few group diffusion theory computer program that determines the nodal flux and power distributions in a fuel bundle. The rod-by-rod thermal spectra are calculated by the leakage-dependent integral transport method. Leakage iterations between diffusion theory and thermal spectrum calculations are carried out to generate thermal broad-group diffusion parameters. In the epithermal and fast energy range, the level-wise resonance integrals are calculated by an improved intermediate resonance approximation in which the intermediate resonance parameters are fuel-rod-temperature dependent. An improved burnup integration scheme is employed in poison burnup calculations.

ACKNOWLEDGMENTS

The following people deserve credit for their major contributions to the development and maintenance of the Three-Dimensional BWR Core Simulator:

R. L. Crowther, H. M. Johnson, C. L. Martin and J. P. Rea. The lattice physics methods described herein were developed as the result of a joint project between General Electric and Toshiba. The major contributors include M. Yamamoto, H. Mizuta, K. Makino, H. Kawamura and S. Tatemichi of NAIG and Toshiba, and S. C. Bhatt, R. T. Chiang, S. P. Congdon, R. L. Crowther, M. B. Goldstein, C. L. Martin, C. T. McDaniel and P. T. Vu of General Electric. This report was compiled through the joint efforts of R. T. Chiang, S. P. Congdon, C. L. Martin and W. A. Zarbis.

## 1. INTRODUCTION

The core of a boiling water reactor (BWR) is a large, three-dimensional, heterogeneous system comprising hundreds of fuel bundles in various kinds of bundle designs, control states, void conditions, and accumulated exposures. The inherent complexity of the system makes it impractical to utilize explicit transport theory methods (e.g., the Monte Carlo Method) to model all details of the whole heterogeneous core at a single stage. Thus, the modeling is broken into two stages: the first is bundle modeling, and the second is coarse-mesh core modeling based on input from bundle modeling.

In Section 2 the methods used to model the reactor core are presented. Section 3 discusses the lattice physics methods used to perform fuel bundle calculations. A thermal-hydraulics model is coupled to the core nuclear model to determine flow and void distributions. This model is presented in Section 4. Section 5 describes the qualification of these methods against data taken at operating BWRs.



## 2. THREE-DIMENSIONAL NUCLEAR MODEL

The nuclear model is based on coarse nodal, one-group, static diffusion theory. The mesh points are distributed approximately every two fast neutron mean free paths. Because of the short thermal neutron mean free path in a water reactor, most neutron diffusion takes place at high neutron energy. Therefore, the model is oriented toward accurate representation of fast neutron diffusion.

It is important to account for lattice fine structure in determining nuclear data for the coarse-mesh global model. Separability is assumed for lattice cells consisting of one or more fuel bundles. The nuclear input preparation is performed by detailed calculations for the lattice cells or fuel types. Coarse-mesh diffusion parameters are fit parametrically as a function of moderator density, exposure, control, and moderator density history. (Moderator density history accounts for spatial isotopic concentrations which are affected by the neutron spectrum during burnup; the spectrum, in turn, is sensitive to moderator density.) These parametric calculations produce isotopic compositions and three-group cross-section data homogenized over the lattice cell. The methods and procedures used in the lattice model are described in Section 3. A data reduction program processes these data into correlations and tables used in the BWR Simulator.

The nuclear model includes representation of Doppler broadening as a function of effective average fuel temperature. Xenon poisoning is considered with the spatial xenon concentration calculated for equilibrium conditions or input specified for nonequilibrium conditions. Provisions are also made to account for the reactivity effect of crud deposited on fuel rods.

Convergence of inner flux iterations is achieved through the use of successive over-relaxation (SOR). Outer void loops are converged with an under-relaxation technique. A power-exposure iteration option is available (Reference 2-1). Neutron flux is converted to fission power for thermal-hydraulic coupling.

Spatial isotopic concentrations are calculated for fuel cycle analysis. Simulated in-core instrument readings can also be calculated.

2.1 COARSE NODAL, ONE-GROUP DIFFUSION THEORY

The derivation of the nodal equations begins with the three-group neutron diffusion equations:

$$-\nabla \cdot D_1 \nabla \phi_1(\underline{r}) + \Sigma_1 \phi_1(\underline{r}) = \frac{1}{\lambda} \sum_g v_g \Sigma_{fg} \phi_g(\underline{r}) \quad (2-1)$$

$$-\nabla \cdot D_2 \nabla \phi_2(\underline{r}) + \Sigma_2 \phi_2(\underline{r}) = \Sigma_{s\ell 1} \phi_1(\underline{r}) \quad (2-2)$$

$$-\nabla \cdot D_3 \nabla \phi_3(\underline{r}) + \Sigma_3 \phi_3(\underline{r}) = \Sigma_{s\ell 2} \phi_2(\underline{r}) \quad (2-3)$$

where

$\phi_g(\underline{r})$  = neutron flux;

$D_g$  = diffusion coefficient;

$\Sigma_g$  = removal cross section;

$\Sigma_{s\ell g}$  = slowing-down cross section;

$v_g$  = number of neutrons per fission;

$\Sigma_{fg}$  = fission cross section; and

$\lambda$  = effective multiplication constant.

Define

$$k \equiv \frac{1}{\Sigma_1} \sum_g v_g \Sigma_{fg} \phi_g / \phi_1 \quad (2-4)$$

$$B_1^2 \equiv \frac{k/\lambda - 1}{M_1^2} \quad (2-5)$$

$$M_1^2 \equiv D_1/\Sigma_1 \quad (2-6)$$

Then the equation for the fast group becomes:

$$\frac{1}{D_1} \nabla \cdot D_1 \nabla \phi_1(\underline{r}) + B_1^2 \phi_1(\underline{r}) = 0. \quad (2-7)$$

This equation depends implicitly on the resonance (group 2) and thermal (group 3) fluxes through the definition of  $B_1^2$ . These fluxes must be approximated in some way in order for the diffusion calculation to be limited to one group. The procedure used is to assume that the geometric bucklings in all three energy groups are the same.

$$\frac{\nabla \cdot D_3 \nabla \phi_3}{D_3 \phi_3} \approx \frac{\nabla \cdot D_2 \nabla \phi_2}{D_2 \phi_2} \approx \frac{\nabla \cdot D_1 \nabla \phi_1}{D_1 \phi_1} = -B_1^2 \quad (2-8)$$

Using these approximations, the resonance-to-fast and thermal-to-resonance flux ratios may be obtained from Equations 2-2 and 2-3:

$$\phi_2/\phi_1 \approx \frac{\Sigma_{s21}/\Sigma_2}{1 + M_2^2 B_1^2} = \frac{\phi_2^\infty/\phi_1^\infty}{1 + M_2^2 B_1^2} \quad (2-9)$$

$$\phi_3/\phi_2 \approx \frac{\Sigma_{s32}/\Sigma_3}{1 + M_3^2 B_1^2} = \frac{\phi_3^\infty/\phi_2^\infty}{1 + M_3^2 B_1^2} \quad (2-10)$$

where  $\phi_1^\infty$ ,  $\phi_2^\infty$ , and  $\phi_3^\infty$  denote the fluxes in an infinite system.

These results are then substituted into Equations 2-4 and 2-5 to obtain:

$$B_1^2 \approx \frac{1}{M_1^2} \left[ \frac{1}{\lambda \Sigma_1} \left( \nu \Sigma_{f1} + \left( \nu \Sigma_{f2} + \nu \Sigma_{f3} \frac{\phi_3^\infty/\phi_2^\infty}{1 + M_3^2 B_1^2} \right) \frac{\phi_2^\infty/\phi_1^\infty}{1 + M_2^2 B_1^2} \right) - 1 \right] \quad (2-11)$$

This equation is solved by multiplying through by the factors involving  $B_1^2$  and then eliminating terms of order  $B_1^4$  and  $B_1^6$ , yielding:

$$\lambda \left( 1 + M^2 B_1^2 \right) = k_\infty + A_\infty B_1^2 \quad (2-12)$$

or

$$B_1^2 = \frac{k_\infty/\lambda - 1}{M^2 - A_\infty/\lambda} \quad (2-13)$$

where the following definitions have been made.

$$M^2 \equiv M_1^2 + M_2^2 + M_3^2 \quad (2-14)$$

$$k_\infty \equiv \frac{1}{\Sigma_1} \left( v_{\Sigma_{f1}} + v_{\Sigma_{f2}} \frac{\phi_2^\infty}{\phi_1^\infty} + v_{\Sigma_{f3}} \frac{\phi_3^\infty}{\phi_1^\infty} \right) \quad (2-15)$$

$$A_\infty \equiv \frac{1}{\Sigma_1} \left( v_{\Sigma_{f1}} \left( M_2^2 + M_3^2 \right) + v_{\Sigma_{f2}} M_3^2 \frac{\phi_2^\infty}{\phi_1^\infty} \right) \quad (2-16)$$

Note that Equation 2-13 is an approximate expression for the buckling, whereas Equation 2-5 is exact.

Equations 2-7 and 2-13 together form the basis for the one-group model. The next step in the derivation is to discretize these equations in the spatial dimension. In order to limit the number of nodes to a practical value, a coarse-mesh approach is adopted with dimensions roughly 6 in. on each edge. A definition of the model used to describe the core geometry is contained in Appendix A.

The first step is to integrate Equation 2-7 over a single node:

$$\frac{1}{\Delta V D_i} \int_{\Delta V} d^3 \underline{r} \nabla \cdot D_i \nabla \phi_i(\underline{r}) + \frac{B_i^2}{\Delta V} \int d^3 \underline{r} \phi_i(\underline{r}) = 0. \quad (2-17)$$

where the subscript referencing the fast group has been eliminated and replaced with a subscript "i" denoting the node under consideration. Making use of Gauss' Theorem:

$$\frac{1}{\Delta V D_i} \int_{S_i} d\underline{S} \cdot D_i \nabla \phi_i(\underline{r}_s) + B_i^2 \bar{\phi}_i = 0 \quad (2-18)$$

where the "bar" over the flux indicates an average over the node.

Performing the integration leads to the following nodal equation:

$$(2-19)$$

$$(2-20)$$

and where the subscript "j" refers to the adjacent nodes and  $h_{ij}$  is defined as the distance between the nodes i and j.

The boundary conditions which are used are of the "mixed" type at the interface between the core and the reflector:

$$D \hat{n} \cdot \nabla \phi(\underline{r}_s) + \Gamma \phi(\underline{r}_s) = 0, \quad \underline{r}_s \in S \quad (2-21)$$

\*General Electric Company Proprietary Information has been deleted.

## 2.2 VOID AND EXPOSURE EFFECTS

The nuclear parameters  $M^2$ ,  $D_1$ ,  $k_\infty$ , and  $A_\infty$  are obtained from the detailed X-Y physics calculations documented in Section 3 and performed for lattice cells (fuel types) normally consisting of one fuel bundle and its surrounding water. These multi-group calculations produce three-group cross sections homogenized over the lattice cell. The data are represented by polynomial fits and by Lagrangian interpolation of tabulated values for each fuel type.

In the solution of the coarse nodal approximation of the one-group diffusion theory model, void, exposure, and fuel type conditions of a node in three-dimensional space are used in the fits and tables to interpret nuclear properties for that node. In this way, void feedback, burnup effects, and heterogeneous fuel loading are taken into account.

Void dependence is represented by the ratio of cell average water density relative to saturated water density used in the lattice cell calculation. This ratio is given by:

$$\frac{\rho}{\rho_f} = 1 + \left( \frac{\rho_g}{\rho_f} - 1 \right) \left[ F \alpha_i + (1-F) \alpha_o \right] \quad (2-22)$$

where

- $\rho$  = cell average water density;
- $\rho_f$  and  $\rho_g$  = saturated liquid and vapor water density, respectively;
- $F$  = volume fraction of water inside the channel relative to total water for the cell;
- $\alpha_i$  = in-channel void fraction; and
- $\alpha_o$  = out-of-channel void fraction.

The parameter U is used to represent relative moderator density for the cell:

$$U = \frac{\rho}{\rho_f} \quad (2-23)$$

Every node in three-dimensional space has a value of U at a given operating point during burnup of the core; therefore, U is an instantaneous relative moderator density. By averaging U with respect to exposure of the node E, history-dependent relative moderator density is defined as:

$$U_H = \frac{\int U \, dE}{\int dE} \quad (2-24)$$

Spatial isotopic concentrations in the cell are dependent upon the neutron spectrum during burnup, which is expressed as a function of  $U_H$ . The spectrum at any point in exposure is expressed as a function of U.

Void distribution in the core is determined by the thermal-hydraulics model according to power and flow distributions and core average pressure. Exposure is accumulated during plant simulation by knowing power and fuel weight distributions and the time of operation (or core average accumulated exposure). Local U,  $U_H$ , and E conditions determine nuclear properties of a node according to correlations of the lattice cell physics calculations. For each fuel type,  $k_\infty$  is dependent upon U,  $U_H$ , and E, while  $M^2$ ,  $D_1$ , and  $A_\infty$  are expressed in terms of U only.

### 2.3 CONTROL ROD EFFECTS

The detailed lattice cell calculations described in Section 3 are performed with the control rod in or out. Therefore, nuclear parameters are obtained for each fuel type at several void and exposure conditions, controlled and uncontrolled. In the three-dimensional diffusion theory solution, the control rod configuration is accounted for by using controlled or uncontrolled data for each node. If a control rod is only partially inserted into a node, linear averaged nuclear data are used. For each fuel type,  $k_\infty$ ,  $D_1$ , and  $M^2$  are control dependent, while  $A_\infty$  is not.

During plant simulation, control rod maneuvering affects the static power distribution and, therefore, void distribution and exposure accumulation.

#### 2.4 DOPPLER EFFECTS

Fuel temperature (T) affects resonance absorption in uranium and plutonium (the Doppler effect). This is accounted for by making a Doppler reactivity correction to  $k_{\infty}$  at each node in the form:

$$k_{\infty}(T) = k_{\infty}(T_0) \left[ 1 + \frac{\Delta k}{k}(T) \right] \quad (2-25)$$

where  $T_0$  represents base fuel temperature, and

$$\frac{\Delta k}{k}(T) = C_T \left[ \sqrt{T} - \sqrt{T_0} \right]. \quad (2-26)$$

The Doppler coefficient  $C_T$  is dependent upon control and U for each fuel type. It is determined by lattice cell physics calculations performed parametrically as a function of fuel temperature.

The effective fuel temperature (T) is represented as a function of power for each fuel type. This relationship is obtained by detailed heat conduction solutions using appropriate thermal conductivity and fuel rod diameter. Knowing the power and void distributions, Equation 2-26 gives Doppler reactivity for each node.

#### 2.5 XENON EFFECTS

Xenon is a fission product which acts as a strong absorber of thermal neutrons. It is produced directly from fission and indirectly by decay of iodine. The xenon poisoning effect is accounted for by making a xenon reactivity correction to  $k_{\infty}$  at each node in the form:

$$k_{\infty}(N_x) = k_{\infty}(N_x = 0) \left[ 1 + \frac{\Delta k}{k}(N_x) \right] \quad (2-27)$$

where  $N_x$  represents xenon concentration. Xenon reactivity is expressed by:

$$\frac{\Delta k}{k} (N_x) = C_x \frac{N_x}{N_x^r} \quad (2-28)$$

where  $N_x^r$  represents xenon concentration at rated power density. The xenon coefficient  $C_x$  is evaluated at rated power density and represented as a function of exposure for each fuel type.

Neglecting absorption in iodine, the static (equilibrium) xenon concentration may be expressed by:

$$N_x = \frac{(\gamma_x + \gamma_i) f}{\lambda_x + \sigma_x \phi_t} \quad (2-29)$$

where

- $\gamma$  = fission yield;
- $i$  = iodine;
- $f$  = fission rate;
- $\lambda$  = decay constant;
- $\sigma$  = microscopic absorption cross section; and
- $\phi_t$  = thermal flux.

Therefore,

$$\frac{N_x}{N_x^r} = \frac{f}{f^r} \frac{(g + 1)}{\left( g + \frac{\phi_t}{\phi_t^r} \right)} \quad (2-30)$$

where  $r$  represents conditions at rated power density, and

$$g = \frac{\lambda_x}{\sigma_x \phi_t^r} \quad (2-31)$$

Letting  $p$  be nodal power density relative to rated, and assuming

$$p = \frac{f}{f^r} = \frac{\phi_t}{\phi_t^r} \quad (2-32)$$

leads to

$$\frac{\Delta k}{k} (N_x) = C_x p \frac{(g + 1)}{(g + p)} \quad (2-33)$$

The parameter  $g$  is evaluated at average (rated) conditions for each fuel type. Knowing power and exposure distributions, Equation 2-28 gives xenon reactivity for each node.

## 2.6 CRUD EFFECTS

Crud buildup on fuel rod surfaces as a result of prolonged operation with slight impurities in the coolant water can act as a neutron absorber. The reactivity effect of crud is accounted for by making a correction to  $k_\infty$  at each node in the form:

$$k_\infty (\text{crud}) = k_\infty (\text{no crud}) \left[ 1 + \frac{\Delta k}{k} (\text{crud}) \right] \quad (2-34)$$

where  $\frac{\Delta k}{k} (\text{crud})$  is a function of the instantaneous relative moderator density  $U$  for each fuel type and the thickness of crud buildup at a given node.

Crud buildup is represented by either of two simple models. The first expresses the mils/year accumulated as a function of flow rate, in-channel void fraction, and average cladding heat flux for each channel and each axial level. An exponential term permits increased crud buildup at the channel inlet. The second model is similar, but allows identification of two specific types of crud in the feedwater flow. Integrating mils/year over core life yields crud thickness.

2.7 CONVERSION OF FLUX TO POWER

Solution of the one-group diffusion theory model (Equation 2-9), using nodal-dependent values for the nuclear parameters  $k_{\infty}$ ,  $M^2$ ,  $D_1$ , and  $A_{\infty}$ , yields the neutron flux  $\bar{\phi}_i$  at each node. Neutron flux must be converted to fission power to determine how much heat is being produced to evaluate thermal-hydraulic feedback effects such as flow, void, and fuel temperature. The equation for power is made consistent with the one-group model in the following derivation.

The power at each node "i" in the core is determined by integrating the fission density over the nodal volume:

$$P_i = \frac{1}{\Delta V} \int d^3 \underline{r} \epsilon_i \sum_g \Sigma_{fg_i} \phi_{g_i}(\underline{r}) \quad (2-35)$$

$$= \epsilon_i \sum_g \Sigma_{fg_i} \bar{\phi}_{g_i} \quad (2-36)$$

where  $\Sigma_{fg}$  is the fission cross section and  $\epsilon_i$  is a conversion factor relating fissions to energy. In this model,  $\epsilon_i$  is assumed to be constant throughout the core and arbitrarily set to 1. The power is normalized such that the average nodal power is 1.

The average number of neutrons produced by fission  $\bar{\nu}_i$  is estimated as follows:

$$\bar{\nu}_i \equiv \frac{\sum_g \nu_{g_i} \Sigma_{fg_i} \bar{\phi}_{g_i}}{\sum_g \Sigma_{fg_i} \bar{\phi}_{g_i}} \cong \frac{\sum_g \nu_{g_i} \Sigma_{fg_i} \bar{\phi}_{g_i}^{\infty}}{\sum_g \Sigma_{fg_i} \bar{\phi}_{g_i}^{\infty}} \quad (2-37)$$

This is a very good approximation, since  $\nu_{g_i}$  is not strongly group dependent. Then making use of Equation 2-4,

$$P_i = \frac{1}{\bar{v}_i} \sum_g v_{g_i} \Sigma_{fg_i} \bar{\phi}_{g_i} = \frac{\Sigma_{1i} k_i}{\bar{v}_i} \bar{\phi}_{1i} . \quad (2-38)$$

In this method,  $k_i$  is evaluated by adding a spectral mismatch correction,  $\Delta k_i$ , to  $k_{\infty i}$ :

$$k_i = k_{\infty i} + \Delta k_i \quad (2-39)$$

This spectral mismatch correction is assumed to be proportional to the difference between the spectral index of each node "i" and a weighted spectral index of its neighbors.

Once the nodal flux is determined by solution of Equation 2-9, the power at each node is evaluated using the above expression.  $\Sigma_1$  is represented as a function of instantaneous relative moderator density U for each fuel type, while  $\bar{v}$  is a function of exposure E for each fuel type. The spectral index is a function of both exposure and relative moderator density for each fuel type.

## 2.8 ISOTOPIC TRACKING

Isotopic tracking is performed by expressing total uranium, U-235, total plutonium, and fissile plutonium weight fractions relative to total heavy metal as functions of exposure E, history-dependent relative moderator density UH, and relative power density p for each fuel type. Knowing E, UH, and p at each node, these four isotopic weight fractions may be evaluated.

To provide accurate representation of isotopic concentrations, the functional dependence is derived from physical principles. First-order expressions are obtained, with parameters determined from detailed lattice cell physics calculations.

## 2.9 TRAVELING IN-CORE PROBE (TIP) CALCULATION

The BWR incorporates TIP and fixed monitors to measure operating power distributions. These monitors are located in the bypass flow gap at the corners of four bundle cells. The monitor reading is influenced by each of these

surrounding bundles. The BWR Simulator calculates predicted TIP readings as a function of four-bundle cell averaged one-group flux and in-channel void fraction. These calculated TIP readings can be compared with measured TIP data to qualify the accuracy of the analytical model. Also, the calculated TIP results can be used in design to predict monitor response during actual BWR operation.

The TIP model represents a fission chamber monitor having a response proportional to the number of fissions:

$$(2-40)$$

where  $C$  is a proportionality constant, and the fission rate is evaluated at the chamber location. The one-group flux expressed by Equation 2-9 is averaged over the four nodes horizontally surrounding the chamber location and is represented by  $\bar{\phi}$ . Equation 2-40 may be rewritten in terms of  $\bar{\phi}$  as:

$$(2-41)$$

A series of detailed lattice cell physics calculations have been performed to evaluate the dependence of  $TIP/\bar{\phi}$  as a function of in-channel voids, control blades, etc.

$$(2-42)$$

Knowing nodal values of  $\phi$  and  $\alpha_i$ , the simulated monitor reading may be calculated at any TIP location.

## 2.10 POWER-VOID ITERATION

For a given control rod pattern and exposure distribution, material buckling  $B^2$  depends upon the thermal-hydraulic feedback effects of moderator density, fuel temperature and possible crud deposition. Equilibrium xenon distribution is another feedback mechanism. If  $B^2$  is known (or assumed known) at every node, solution of the one-group diffusion theory model (Equation 2-9) yields the flux distribution. This solution involves inner iterations to determine the fundamental mode flux and effective multiplication constant  $k$ .

Once the flux distribution is determined, fission power distribution is given by Equation 2-38. The power distribution affects thermal-hydraulics in the reactor. In particular, fission power determines fuel temperature and heat flux to the moderator. Fuel temperature sets the amount of Doppler feedback according to Equation 2-26. Heat flux affects the amount of boiling in the channel, which determines moderator density feedback and channel pressure drop. Flow into each channel must be distributed to balance the pressure drop across all channels. Equilibrium xenon feedback is expressed in terms of relative power distribution by Equation 2-33.

The resulting feedback effects may not be the same as originally assumed in the determination of material buckling  $B^2$ . In this case, flux must be reevaluated to represent the new  $B^2$  distribution. This defines an outer loop iteration, which must be continued until the fission power distribution is in equilibrium with the distribution of feedback effects (power-void iteration). The iteration is represented schematically in Figure 2-1.

After power is calculated and before performing additional flux iterations (if required), a neutron balance calculation is performed to improve the estimate of effective multiplication constant  $k$ .

Figure 2-1. Power-Void Iteration Flow Chart

## 2.11 HALING POWER-EXPOSURE ITERATION

The power-exposure iteration provides an end-of-cycle (EOC) state for which the power shape is constant during burnup. This constant power distribution yields a nearly optimum burnup distribution throughout the entire cycle.

The problem is to determine the relative distribution of accumulated exposure  $H_{ijk}$ , assuming burnup with a constant power shape, such that the relative power distribution evaluated using the resulting end-of-cycle exposure distribution is equal to  $H_{ijk}$ . The relative distribution of interest is defined by:

$$H_{ijk} = \frac{E_{ijk}^{EOC} - E_{ijk}^{BOC}}{\overline{\Delta E}} \quad (2-43)$$

where EOC and BOC indicate end-of-cycle and beginning-of-cycle, respectively, and  $\overline{\Delta E}$  is the core average exposure step to go from BOC to EOC. The power-exposure iteration procedure is represented schematically in Figure 2-2.

Normally it is desired to converge on the end-of-cycle state having a desired effective multiplication constant (e.g., a critical reactor with all rods out at EOC). This is accomplished by adjusting  $\overline{\Delta E}$  until the desired  $k^{EOC}$  is achieved.

## 2.12 REFERENCES

- 2-1. R.K. Haling, "Operating Strategy for Maintaining an Optimum Power Distribution Throughout Life", Proceedings of the American Nuclear Society Topical Meeting on Nuclear Performance of Power Reactor Cores (TID-7672) (September 1963).



Figure 2-2. Power-Exposure Iteration Flow Chart



### 3. DETAILED LATTICE PHYSICS METHODS

This section describes the process of accounting for the lattice fine structure in determining nuclear data. This data is then used as input into the three-dimensional coarse-mesh core calculations documented in Section 2. Due to the differences in bundle design, control state, void condition and accumulated exposure, bundle nuclear properties in a core are actually nonuniform both in transverse and axial directions. As a result, the neutron behavior in each axial segment of a bundle is determined not only by the nuclear properties of that segment but also by the nuclear properties of adjacent segments of that bundle and neighboring bundles. The calculation of the influence of neighboring bundles is very difficult because each bundle can potentially undergo a wide spectrum of environments, depending on its location and core operating history. However, this influence is generally small. To model the bundle, an approximation is made to account for the influence of neighboring bundles in the core simulator and to generate homogenized cross sections. This approximation is made by assuming that the bundle is located in an infinite, periodic lattice along the transverse directions and is uniform and infinitely long along the axial direction.

As a result of the preceding approximation, a bundle can be simulated as an "isolated" two-dimensional heterogeneous system that may comprise fuel rods, water rods, burnable poison (gadolinia), in-channel water, channel, out-channel water, and control rod (Figure 3-1). The bundle modeling is then further divided into two stages: (1) the fuel rod cell and external region modeling by using transport theory methods, and (2) the coarse-mesh bundle modeling based on cell homogenization and diffusion theory methods.

#### 3.1 GENERAL DESCRIPTION OF SOLUTION TECHNIQUES

The solution techniques begin with the generation of thermal broad-group neutron cross sections for all homogenized fuel rod cells and external regions in a bundle. In the thermal energy range, the rod-by-rod thermal spectra are calculated by a method similar to the THERMOS formalism (Reference 3-1). The major difference is that neutron leakage from rod to rod is taken into account.

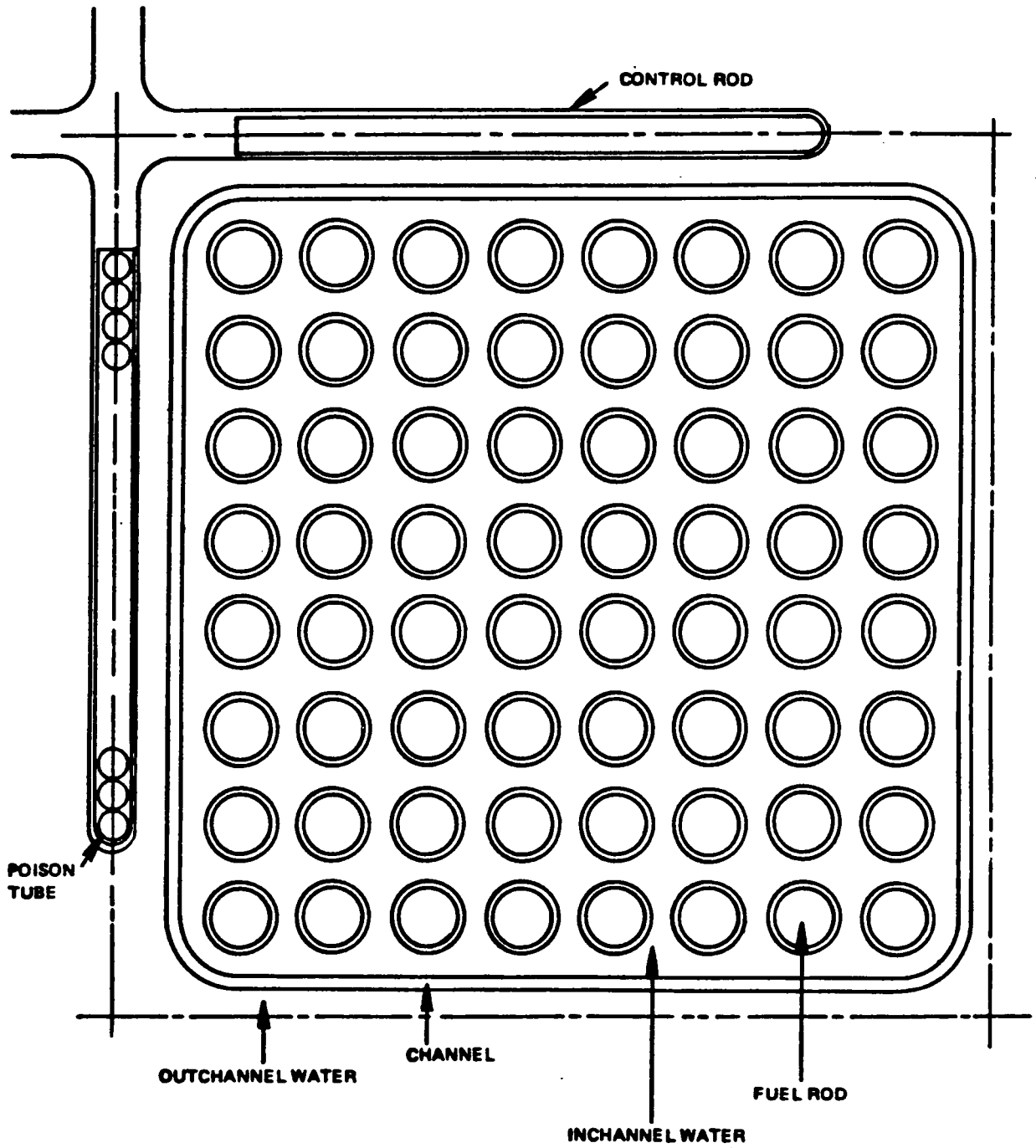


Figure 3-1. Bundle Configuration

The second step is to generate the cell- and region-homogenized cross sections for the fast and epithermal broad groups. In the epithermal and fast energy range, the level-wise resonance integrals are calculated by an improved IR (intermediate resonance) approximation in which the IR parameters are fuel-rod-temperature dependent. In addition, the fuel rod escape probability is calculated according to a treatment by Mizuta (Reference 3-2).

The third step utilizes the cross sections generated in steps one and two in a two-dimensional, coarse-mesh, broad-group, diffusion-theory calculation to determine the nodal flux and power distributions in the bundle.

The fourth and final step is to perform the nuclide depletion calculation. In the depletion calculation, 100 nuclides are treated, including 25 fissile and fertile nuclides and up to 48 fission products plus one pseudo fission product. An improved burnup integration scheme is employed which avoids numerical problems associated with the equations encountered in poison burnup calculations.

The preceding steps are repeated for each burn step until all given burn steps are completed.

### 3.2 THERMAL NEUTRON SPECTRUM AND DIFFUSION PARAMETER CALCULATIONS

In this section, the generation of thermal cross sections and diffusion coefficients is discussed. This process includes the condensation of thermal cross-section library from 30 groups to 16 groups, the calculation of leakage-dependent region-wise neutron spectrum, the generation of thermal

leakage-dependent region-wise neutron spectrum, the generation of thermal homogenized diffusion parameters, and  $P_1$ -blackness theory for strong absorption mediums.

### 3.2.1 Thermal Library Condensation

The conventional library for thermal spectrum calculations is composed of 30-group thermal cross sections. A properly condensed 16-group (group structure is shown in Table 3-1), rather than a 30-group, thermal library, is sufficient for use to calculate the thermal spectrum correctly.

The fluxes for the group condensation of cross sections from 30 to 16 groups are calculated by using the THERMOS (Reference 3-1) method for the averaged regular and the averaged Gd fuel rod cells. Each averaged cell is assumed to have two regions (fuel region and cladding-moderator homogenized region) in the radial direction and to be infinitely long in the axial direction.

### 3.2.2 Thermal Neutron Spectrum Calculation

The integral transport theory method has been widely utilized for calculating thermal neutron spectra in reactor lattices. The THERMOS computer code (based on this method) was introduced by Honeck in 1961. The integral transport method has continued to be used along with two improvements: (1) the collision probability is calculated more accurately, and (2) the reflecting boundary condition is generalized to the albedo (or leakage-dependent) boundary condition.

#### 3.2.2.1 Integral Transport Theory

Following the Wigner-Seitz cell approximation, each fuel rod and its surrounding cladding and moderator are represented by an equivalent cylindrical cell as shown in Figure 3-2.

The integral transport form of the neutron balance equation with isotropic scattering and source in a unit cell is given by:

Table 3-1  
GROUP STRUCTURE OF 16-GROUP THERMAL LIBRARY

Group	Upper Boundaries		
	Velocity, v (Units of 2200 m/sec)	Lethargy, u (u=0 at 10 MeV)	E (eV)
1	0.55	20.99	$7.65 \times 10^{-3}$
2	0.95	19.90	$2.28 \times 10^{-3}$
3	1.35	19.20	$4.61 \times 10^{-2}$
4	1.66	18.78	$6.97 \times 10^{-2}$
5	1.91	18.50	$9.23 \times 10^{-2}$
6	2.195	18.22	0.122
7	2.36	18.08	0.141
8	2.55	17.92	0.165
9	2.77	17.76	0.194
10	3.025	17.58	0.232
11	3.32	17.39	0.279
12	3.66	17.20	0.339
13	4.05	17.00	0.415
14	4.495	16.79	0.511
15	5.00	16.58	0.633
16	5.57	16.36	0.785

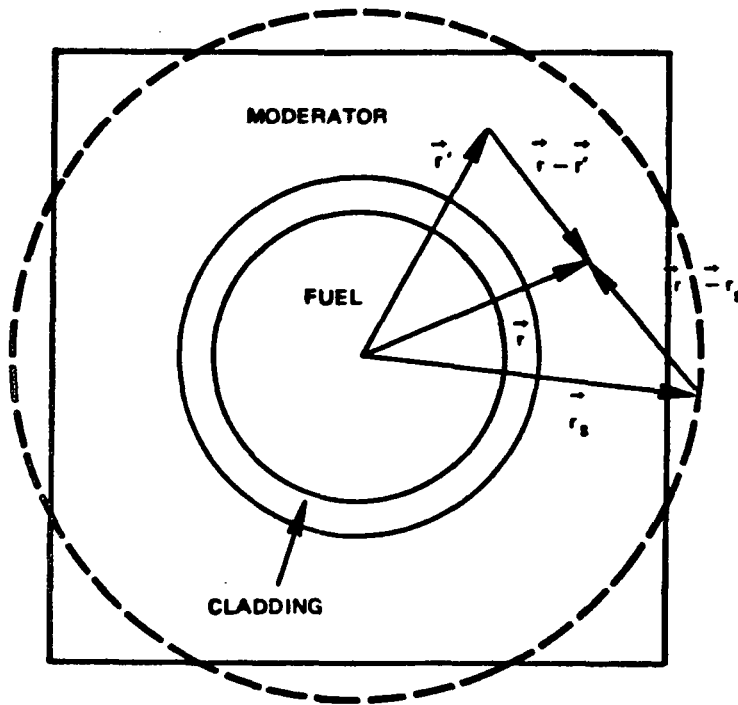


Figure 3-2. An Equivalent Fuel Cell

$$\Sigma_T(\vec{r}, E) \phi(\vec{r}, E) = \int_V dV' P(\vec{r}' \rightarrow \vec{r}, E) \left\{ \int_0^{E_c} dE' \Sigma_S(\vec{r}', E' \rightarrow E) \phi(\vec{r}', E') \right. \\ \left. + Q(\vec{r}', E) \right\} + \int_S dS \hat{n} \cdot \vec{J}_-(\vec{r}_S, \hat{\Omega}_S, E) P(\vec{r}_S \rightarrow \vec{r}, E) \quad (3-1)$$

where

$$P(\vec{r}' \rightarrow \vec{r}, E) = \frac{\Sigma(\vec{r}, E)}{4\pi |\vec{r} - \vec{r}'|^2} \exp \left[ - \int_0^{|\vec{r} - \vec{r}'|} \Sigma \left( \vec{r} - R' \frac{(\vec{r} - \vec{r}')}{|\vec{r} - \vec{r}'|} \right) dR' \right].$$

and

$\Sigma_S(\vec{r}', E' \rightarrow E)$  = the scattering kernel

$Q(\vec{r}', E)$  = the slowing-down source

$P(\vec{r}' \rightarrow \vec{r}, E)$  [or  $P(\vec{r}_S \rightarrow \vec{r}, E)$ ] = the transport kernel

$\vec{J}_-(\vec{r}_S, \hat{\Omega}_S, E)$  = the incoming surface current

$\vec{r}$  = the position vector inside the cell

$\vec{r}_S$  = the position vector on the boundary surface

$E_c$  = the upper thermal cutoff energy

$\hat{\Omega}_S = (\vec{r} - \vec{r}_S) / |\vec{r} - \vec{r}_S|$

$\hat{n}$  = the outer normal direction of boundary surface.

Physically, the left-hand side of Equation 3-1 is the collision removal term for neutrons with energy  $E$  at position  $\vec{r}$ , the first term on the right-hand side is the corresponding source term from all other parts inside the cell, and the second term on the right-hand side represents the surface source term.

The cell is divided into subregions composed of constant cross-sections, then integrated over the volume element  $V_n$  with the assumption of isotropic incoming surface current. The conventional flat flux and flat source approximation is then applied and the result is discretized into the multigroup form. The incoming partial current  $J^-$  is expressed in terms of the net cell leakage and the surface-to-surface transport probability.

#### 3.2.2.2 Surface Leakage

(3-2)

### 3.2.3 Thermal Homogenized Cross Section and Diffusion Coefficient Generation

The homogenized cross sections are formulated by preserving region-wise, thermal reaction rates as:

$$\Sigma_x^j = \frac{\sum_{i,j,k} N_i^{j,k} \sigma_{x,g}^{i,j,k} \phi_g^{j,k} \Delta v_g V_k}{\sum_{k,g} \phi_g^{j,k} \Delta v_g V_k}, \quad x = T, tr, f, a \quad (3-3)$$

where

- $N_i^{j,k}$  = atom density of i-th isotope in k-th subregion of j-th region;
- $V_k$  = k-th volume element;
- $g$  = g-th fine group;
- $\Delta v_g$  = g-th speed interval; and
- $x$  = type of reaction -- total (T), transport(tr), fission (f), or absorption (a).

The homogenized diffusion coefficients are expressed in terms of the transport cross sections and are determined first by energy group condensation:

$$\Sigma_{tr}^{j,k} = \frac{\sum_g \phi_g^{j,k} \Delta v_g}{\sum_g \phi_g^{j,k} \Delta v_g / \Sigma_{tr,g}^{j,k}} \quad (3-4)$$

then by spatial summation:

$$D_j = \frac{\sum_k \phi_{jk} V_k}{3 \sum_k \sum_{tr}^{j,k} \phi_{j,k} V_k} \quad (3-5)$$

where

$$\phi_{jk} = \sum_g \phi_g^{j,k} \Delta v_g.$$

The preceding expressions for the homogenized thermal diffusion parameters cannot be used for control blades, which are composed of strong absorption material. Special treatment is given in the next subsection for this kind of material.

#### 3.2.4 P<sub>1</sub> Blackness Theory

The effective diffusion parameters in a strong absorption medium such as a control blade can be derived by utilizing P<sub>1</sub> blackness theory (Reference 3-3 and 3-4) in slab geometry. P<sub>1</sub> blackness theory comprises three steps: (1) in the black (i.e., high absorbing) region is treated by transport theory with the boundary conditions as linear functions of the direction cosine  $\mu$ ; (2) the finite-difference form of the diffusion equation for the black region is then derived from the transport equation by using the standard P<sub>1</sub> approximation; and (3) the employment of the boundary conditions to the finite-difference equations yields the effective diffusion parameters.

### 3.3 FAST AND EPITHERMAL SPECTRUM AND DIFFUSION PARAMETER CALCULATIONS

This section presents a discussion of the generation of fast and epithermal cross sections and diffusion coefficients. This process includes the consideration of Dancoff factors, the calculation of resonance cross sections, the determination of heterogeneity correction factors from averaged-fuel-rod-cell transport calculation, and the fine-group transport calculation for a one-dimensional equivalent bundle.

#### 3.3.1 Dancoff Factor Calculation

Dancoff factors (Reference 3-5) are used to determine the shadowing effect on incident neutrons to a fuel rod due to the neighboring rods. Dancoff

factors are calculated for each individual fuel rod and include the effects of cladding.

Due to the presence of the water rods, channel box, water gap, and control blade in the BWR lattice, the number of various different kinds of Dancoff pairs may be as many as 25 (Figure 3-3).

### 3.3.2 Resolved Resonance Range Approximation

The resonance absorption of heavy nuclides, especially U-238, is a major factor in determining the neutron multiplication factor of a light water reactor. The resonance cross-sections are calculated using an improved intermediate resonance (IR) approximation by Mizuta (Reference 3-2). The improvements include: (1) temperature dependence of the IR parameters; (2) interference between the potential scattering and the resonance scattering; and (3) improved A-factor in the Wigner rational approximation for the fuel escape probability.

### 3.3.3 Unresolved Resonance Treatment

The average neutron energy decrement per collision is much larger than the average level spacing in the unresolved resonance region; therefore, narrow resonance approximation is applied for unresolved resonance treatment. Moreover, since the neighboring resonance peaks are unresolved with each other, the reduced neutron widths are assumed to be distributed according to the Porter-Thomas distribution:

$$P(y) = \frac{e^{-y/2}}{\sqrt{2\pi y}},$$

where  $y$  is the ratio of each individual reduced width to the average reduced width.

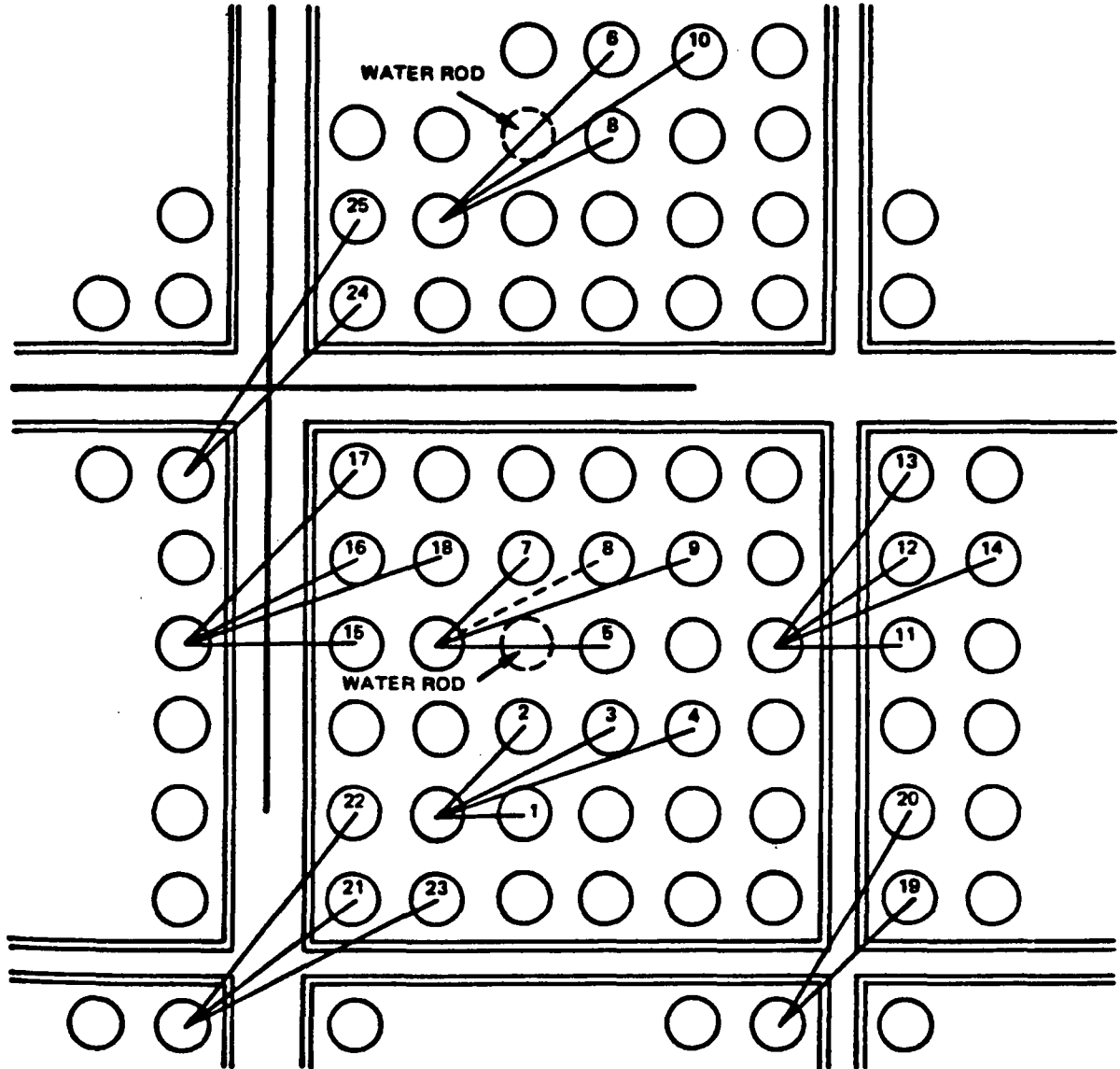


Figure 3.3. Various Dancoff Pairs in the BWR Lattice

### 3.3.4 Determination of Heterogeneity Correction Factors From Averaged Fuel Rod - Cell Transport Calculation

In the fast and epithermal energy range, the flux distribution is quite flat and near-periodic across various fuel-rod-cell regions inside a fuel bundle because the total neutron mean-free-path is much longer than a single fuel-cell pitch. Hence, the flux variation inside each fuel-rod cell is approximately represented by the flux variation obtained from an averaged fuel-rod-cell transport calculation. The fast and epithermal spatial and the fast spectrum heterogeneity factors can then be determined from the flux solution of the averaged fuel-rod-cell transport calculation.

### 3.3.5 Fine-Group Transport Calculation for One-Dimensional Equivalent Bundle

The neutron spectrum in various regions of the fuel bundle is required for condensing and homogenizing the fine-group cross sections as described in the thermal energy range. In the fast and epithermal range, the neutron spectrum in the two-dimensional bundle is approximated by the spectrum obtained from a one-dimensional equivalent bundle transport calculation as follows:

The one-dimensional equivalent bundle is established by preserving the hydrogen-to-uranium atom ratio (H/U) of the actual bundle, because the fast and epithermal spectrum is very sensitive to H/U. It includes seven spectrum regions:

### 3.4 BUNDLE FLUX, POWER AND MISCELLANEOUS CALCULATIONS

This section describes the methods for calculating the neutron flux distributions, the power-related distributions, and the bundle-averaged diffusion parameters. Three broad-energy groups are normally used for these bundle calculations. The first group spans the fast energy range from 5.5 keV to 10 MeV, and includes all neutrons born in fission. The second group spans the resonance energy range from 0.6825 eV to 5.5 keV. The third group is the thermal group that includes all neutrons with energies below 0.6825 eV. In addition, the four-broad-group option is also available for the bundle calculations. In this case, the fast group remains the same, the resonance group is divided into two subgroups (from 0.6825 eV to 3.06 eV and from 3.06 eV to 5.5 keV), and the thermal group becomes the fourth group.

#### 3.4.1 Two-Dimensional Few-Group Coarse-Mesh Diffusion Calculation

To prepare for the coarse-mesh diffusion calculation, the following assumptions are made to represent the fuel bundle:

3.4.1.1 Nodal Diffusion Equations

The two-dimensional few-group diffusion equations for the bundle flux calculations are given by:

$$\begin{aligned}
 & - \frac{\partial}{\partial x} D_g(x,y) \frac{\partial}{\partial x} \phi_g(x,y) - \frac{\partial}{\partial y} D_g \frac{\partial}{\partial y} \phi_g + \Sigma_{Rg}(x,y) \phi_g \\
 & = \frac{1}{k} \chi_g \sum_{g'=1}^G \nu_{g'} \Sigma_{fg'}(x,y) \phi_{g'} + \sum_{g'=1}^{g-1} \Sigma_{S,g'g}(x,y) \phi_{g'}, \quad g=1, \dots, G \quad (3-6)
 \end{aligned}$$

where all notations are standard, and no upscattering is assumed. Since each region is homogenized, the nuclear parameters in that region are represented by their homogenized (constant) values; that is,

$$D_g(x,y) = D_g^{i,j}, \quad \Sigma_{Rg}(x,y) = \Sigma_{R,g}^{i,j}, \quad \Sigma_{fg'}(x,y) = \Sigma_{fg'}^{i,j},$$

and

$$\Sigma_{S,g'g}(x,y) = \Sigma_{S,g'g}^{i,j} \text{ in the region confined by } x_{i+1/2} > x > x_{i-1/2}$$

and

$$y_{j+1/2} > y > y_{j-1/2} \text{ as shown in Figure 3-4.}$$

Equation 3-6 is transformed to the finite difference equation, then solved by using the successive over-relaxation iterative method.



Dividing  $F_n$  by the average fission density  $\bar{F}$  yields the relative rod fission density  $\tilde{F}_n$ :

$$\tilde{F}_n = \frac{F_n}{\bar{F}} = \frac{F_n}{\frac{1}{N} \sum_{n=1}^N F_n}, \quad n=1,2,\dots,N.$$

#### 3.4.2.2 Power Distribution

The relative fission-density distribution is sometimes taken approximately as the relative thermal power distribution. However, the actual relative power distribution is different from the relative fission-density distribution because:

- (1) Different fissionable nuclides yield different amounts of energy per fission.
- (2) A fraction of the fission energy is released in the form of gamma rays, which have long mean-free-paths inside a reactor lattice and, therefore, their energy is often deposited far from their original source. This has the effect of spreading the thermal energy inside the lattice and, consequently, reducing the power peaking.
- (3) Neutron capture results in the release of gamma rays, which lose their energy in the same way as the fission gamma rays.

The fission-energy sources can be separated into two types based on their properties. One is the locally deposited fission energy, which is the kinetic energy of various short-ranged particles including fission fragments, fission neutrons, and betas, and the other is the long-ranged gamma ray energy.

The local source of gamma ray energy  $S_{\gamma n}$  is given by:

(3-8)

where  $E_{\gamma fj}$  and  $E_{\gamma cj}$  are the energy released by the fission gammas and capture gammas of the  $j$ -th isotope.

The eight-group gamma number sources are given by:

(3-9)

where  $\chi_{fj}^{gg'}$  ( $\chi_{cj}^{gg'}$ ) is the number of photons emitted in gamma-energy group  $g'$  per unit gamma energy (MeV) due to a fission (capture) occurred in neutron-energy group  $g$  of the  $j$ -th nuclide. The gamma energies are divided into groups with boundaries at 8.5, 6, 4, 3, 2.2, 1.4, 0.75, 0.3, and 0.1175 MeV.

A complex gamma transport calculation is required to obtain the smeared gamma energy distribution. Based on previous transport calculations, the smeared gamma power  $P_{\gamma n}$  in the  $n$ -th rod can be approximately given by:

(3-10)

where  $\bar{S}_{\gamma}$  is the average gamma source, and  $\beta$  is a constant depending on lattice size. Typical values for  $\beta$  are 0.3163 for a 7x7 lattice and 0.3375 for an 8x8 lattice.

The total power  $P_{Tn}$  in the nth rod is the sum of the locally deposited fission power and smeared gamma power:

$$P_{Tn} = P_{Ln} + P_{\gamma n} , \quad (3-11)$$

and the relative power  $\tilde{P}_{Tn}$  is given by:

$$\tilde{P}_{Tn} = \frac{P_{Tn}}{\frac{1}{N} \sum_{n=1}^N P_{Tn}} \quad (3-12)$$

### 3.4.3 Bundle-Averaged Diffusion Parameters

The group-wise bundle-averaged diffusion coefficients and cross sections are calculated by using the conventional flux-weighted expressions, which preserve the bundle reaction rates. These expressions are:

$$D_g = \left[ \frac{\sum_j \phi_{jg} V_j / D_{jg}}{\sum_j \phi_{jg} V_j} \right]^{-1} \quad (3-13)$$

$$\Sigma_{xg} = \frac{\sum_j \Sigma_{xg}^j \phi_{jg} V_j}{\sum_j \phi_{jg} V_j} , \quad x = f, S, R; \quad g = 1, \dots, G$$

where the summation of j is over the whole bundle.

### 3.5 NUCLIDE DEPLETION CALCULATION

The nuclide depletion calculation is discussed in this section. The process includes the introduction of fission-related nuclide chains and the formulation of nuclide depletion equations.

### 3.5.1 Fission-Related Nuclide Chains

There are two types of fission-related nuclide chains: (1) fissionable nuclide and (2) fission product. The relationship among various nuclides in these chains is important for calculating the production and destruction of major nuclides as functions of exposure in a nuclear reactor.

The fissionable nuclide chains are shown in Figure 3-5. The  $\beta$ -decay and radioactive capture (n- $\gamma$  reaction) are two main reactions in these chains. The n-2n reaction and  $\alpha$ -decay also occur, but their contribution to the production and destruction is usually small.

The fission product model contains 29 major fission products and a pseudo fission product representing the contribution from the other minor fission products.

### 3.5.2 Nuclide Depletion in Fuel Rods

For nuclide depletion, each regular fuel rod is assigned a burn region and each Gd fuel rod is divided up into a maximum of 20 (normally 10) burn regions to track the gadolinium isotopes. In each burn region, the nuclide-depletion equations are:

$$\frac{dN_i(t)}{dt} = P_i(t) - L_i(t) , i = 1, 2, \dots, I \quad (3-14)$$

where

$N_i(t)$  = isotope density;

$P_i(t)$  = production rate;

$L_i(t)$  = loss rate; and

subscript "i" represents a nuclide type.



Equation 3-14 is a set of coupled, first-order differential equations that governs the changes of nuclide densities with respect to time in a burn region.

The production rate of the  $i$ -th nuclide is the sum of its total yield from fissions of all fissionable nuclides, the neutron capture rate of its  $k$ -th precursor (which has the same atomic number but with a mass number one unit smaller), and the beta decay rate from its  $m$ -th precursor (which has the same mass number but with an atomic number one unit smaller):

$$P_i(t) = \sum_{j=1}^J Y_i^{(j)} N_j(t) \sum_{g=1}^G \sigma_{fg}^{(j)} \phi_g + N_k(t) \sum_{g=1}^G \sigma_c^{(k)} \phi_g + \lambda_m N_m(t) \quad (3-15)$$

where  $Y_i^{(j)}$  is the fission yield of the  $i$ -th nuclide due to the  $j$ -th fissionable nuclide, and  $\lambda_m$  is the decay constant of the  $m$ -th precursor. The loss rate of the  $i$ -th nuclide is the sum of its decay and absorption rates:

$$L_i(t) = N_i(t) \left[ \lambda_i + \sum_{g=1}^G \sigma_{ag}^{(i)} \phi_g \right]. \quad (3-16)$$

Substituting Equations 3-14 and 3-15 into Equation 3-16 yields:

$$\frac{dN_i(t)}{dt} = \lambda_m N_m(t) - \lambda_i N_i(t) + \sum_{j=1}^J Y_i^{(j)} N_j(t) \sum_{g=1}^G \sigma_{fg}^{(j)} \phi_g + \sum_{g=1}^G \left[ \sigma_{cg}^{(k)} N_k(t) - \sigma_{ag}^{(k)} N_i(t) \right] \phi_g, \quad i=1, 2, \dots, I \quad (3-17)$$

which is a set of coupled, nonlinear, differential equations for nuclide depletion. These depletion equations are solved using the fourth-order Runge-Kutta-Gill numerical integration technique (Reference 3-6).

## 3.6 REFERENCES

- 3-1. H. C. Honeck, "THERMOS: A Thermalization Transport Code for Reactor Lattice Calculations," BNL-5826 (1961).
- 3-2. H. Mizuta, "Analytical Expression for Factor  $\bar{A}$  in Rational Escape Probability," J. Nucl. Sci. Tech., 10, 192 (1973).
- 3-3. C. W. Maynard, Section 3.6, Naval Reactors Physics Handbook, Vol. I, A. Radkowsky, ed., U.S. AEC (1964).
- 3-4. S. P. Congdon and M. P. Mendelson, " $P_N$  Blackness Theory in Plane Geometry," Nucl. Sci. Eng., 33, 151 (1968).
- 3-5. S. M. Dancoff and M. Ginsburg, "Surface Resonance Absorption in a Closed Packed Lattice," CP-2157 (1944).
- 3-6. S. Gill, "Step-by-Step Integration of Differential Equations," Proc. Cambridge Philos. Soc., 47, pp. 96-108 (1950).



#### 4. THERMAL-HYDRAULICS MODEL

Power-void feedback of a BWR core makes the thermal-hydraulic representation of considerable importance to the nuclear calculation. Nuclear parameters and, therefore, the power distribution are sensitive to local steam void content.

Formulas from the 1967 ASME Steam Tables (Reference 4-1) are used to evaluate coolant properties as a function of reactor core pressure and inlet enthalpy. All thermal-hydraulic variables are assumed to vary linearly between nodes, where the nodal representation is the same as that for the neutron flux (Figure A-1 in Appendix A); therefore, the thermal-hydraulic model is consistent with the difference equations used for solution of the nuclear model.

The flow distribution for characteristic parallel channels is determined by balancing core pressure drop. Characteristic channels are determined by combinations of total channel power, axial power shape, inlet orifice design, channel geometry (e.g., number of fuel rods, spacer design, lower and upper tie plate design), and buildup of crud on the fuel rods. The flow into individual channels is obtained by interpolation among characteristic channels of the same geometry and orifice type as a function of radial and axial power factors and crud thickness.

The axial enthalpy and quality distribution is determined for each channel by a nodal energy balance which considers fuel rod heat flux to the coolant, neutron moderation and gamma heating in the coolant and in the flow channel wall, heat transfer through the channel wall to the bypass region, and  $\gamma$ ,  $(n,\gamma)$ , and  $(n,\alpha)$  heating in control blades. The void distribution is given by a void-quality correlation which provides a physically oriented representation of sub-cooled and bulk boiling through a few empirical constants which describe the local flow structure.

Flow-power-void iteration is required to reach an equilibrium condition (Figure 2-1). Once this is obtained, the thermal-hydraulics model enables evaluation of the margin relative to thermal limits.

#### 4.1 FLOW DISTRIBUTION

The purpose of the flow distribution calculation is to determine the distribution of total core inlet flow into individual channels, such that the pressure drop across each channel is the same. This pressure drop is given by a combination of friction, elevation, acceleration, and local losses, which are influenced by coolant density, orificing, lower and upper tie plate design, spacer design, fuel bundle geometry, and crud thickness. Coolant density is determined by pressure, inlet subcooling, and the distribution of steam voids, which is affected by the total power generated in the fuel rods within the channels and by the axial power distribution.

Since current BWR designs have a large number of fuel channels (up to 848), the following steps are used to reduce the computational effort for determining flow distribution:

- (1) Define a limited number of characteristic channels.
- (2) Obtain the flow in each characteristic channel by balancing channel pressure drops while preserving total core flow.
- (3) Calculate the flow in each individual channel of the reactor based upon the variation of that channel relative to the characteristic channels.

Characteristic channels are defined by combinations of the parameters primarily affecting pressure drop:

- (1) total channel power;
- (2) axial power shape;
- (3) crud size;
- (4) orifice size; and

- (5) channel geometry.

The following major assumptions are used to efficiently compute pressure drop and flow for the characteristic channels:

- (1) Total core inlet flow and bypass (leakage) flow (Subsection 4.4) are given.
- (2) All coolant properties are evaluated at the given core average pressure.
- (3) Power shape characteristics are represented by two axial nodes.
- (4) Six axial nodes are used for thermal-hydraulics modeling in the active fuel region.

Figure 4-1 is a schematic of characteristic channel nodalization depicting the active fuel section (which contains heated fuel rods), the unheated section with rods, and the unheated section without rods. Pressure drop for a characteristic channel is determined by summing the following components:

- (1) local loss pressure drop through the orifice;
- (2) acceleration pressure drop due to an area change from the inlet area to the rodded bundle area;
- (3) friction pressure drop in the heated section;
- (4) elevation pressure drop in the heated section;
- (5) acceleration pressure drop due to a density change in the heated section;
- (6) local loss pressure drop through the heated section;

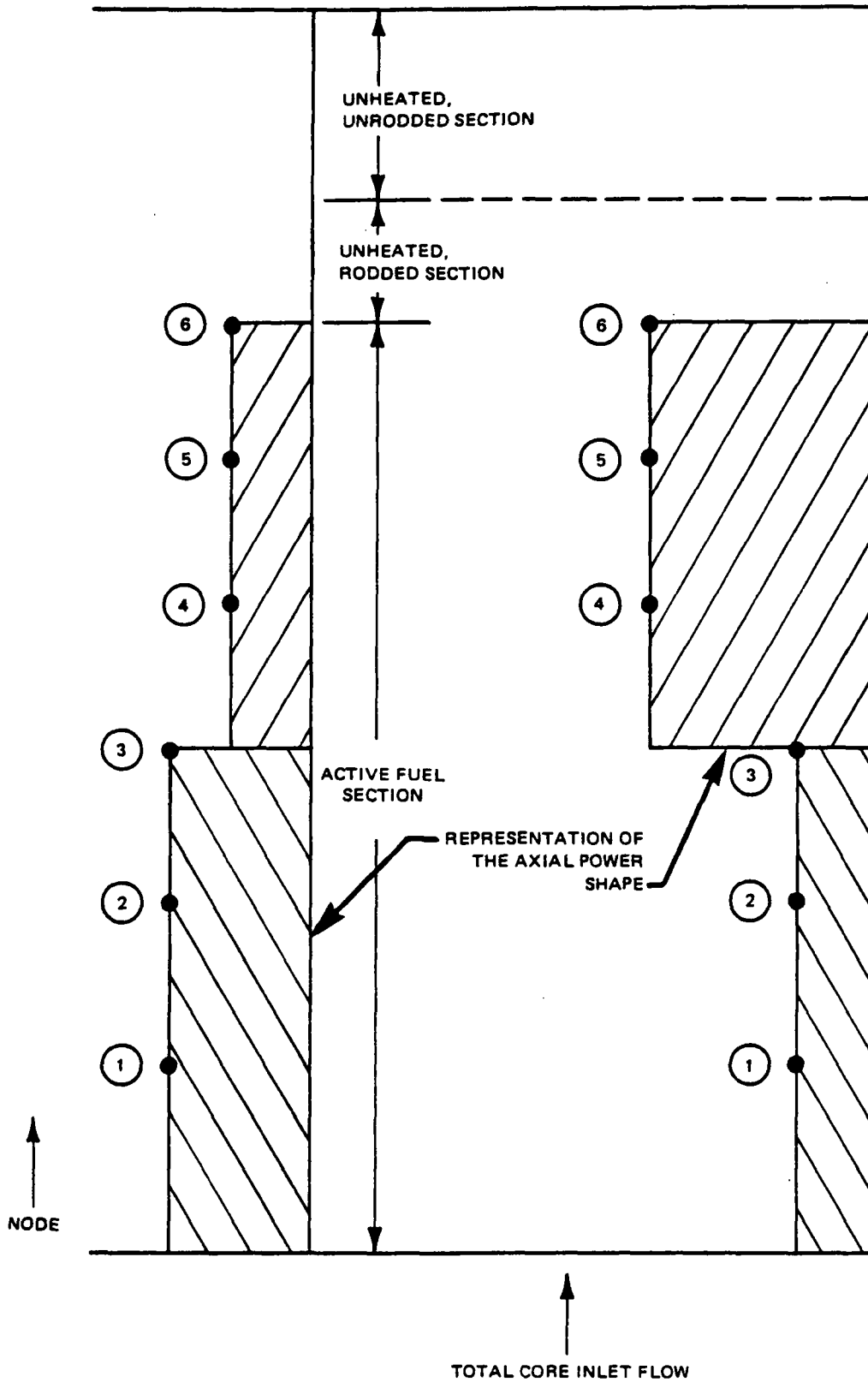


Figure 4-1. Schematic of Characteristic Channel Nodalization

- (7) acceleration pressure drop due to an area change from the rodded bundle area to the outlet area;
- (8) friction pressure drop in the unheated rodded section; and
- (9) elevation pressure drop in the unheated section.

Summarizing, characteristic channel pressure drop is given by:

$$\Delta P_{\text{tot}} = \Delta P_{\text{fri}} + \Delta P_{\text{ele}} + \Delta P_{\text{loc}} + \Delta P_{\text{acc}} \quad (4-1)$$

(4-2)

where

L = length of the flow passage

A = flow area

$D_H$  = hydraulic diameter

$\rho_\ell$  = average liquid density over L (In two-phase flow,  $\rho_\ell$  is saturated liquid density.)

W = mass flow rate for the characteristic channel

f = single-phase friction factor

$\phi_{\text{TPF}}^2$  = two-phase friction multiplier

The single-phase friction factor is calculated from:

(4-3)

where a, b and c are correlation coefficients,  $N_{\text{Re}}$  is Reynold's number evaluated at saturation properties, and  $\epsilon$  is the surface roughness.

(4-4)

The second term in Equation 4-1, elevation pressure drop, is calculated from:

$$\Delta P_{ele} = \Delta Z \bar{\rho} \quad (4-5)$$

where  $\Delta Z$  is the distance over which the elevation pressure drop is calculated and  $\bar{\rho}$  is average density over the distance  $\Delta Z$ . In the subcooled portion of the bundle, average density is:

$$\bar{\rho} = \frac{1}{2} (\rho_Z + \rho_{Z+\Delta Z}) \quad (4-6)$$

In the two-phase portion of the bundle, average density is:

$$\bar{\rho} = (1 - \bar{\alpha}) \rho_f + \bar{\alpha} \rho_g$$

where

$$\bar{\alpha} = \frac{1}{2} (\alpha_Z + \alpha_{Z+\Delta Z}) \quad (4-8)$$

and  $\rho_f$  and  $\rho_g$  are saturated liquid and vapor densities.

The third pressure drop term in Equation 4-1 is the irreversible pressure drop due to local flow disturbances such as fuel rod spacers or area changes in the flow path. The formulation used is:

(4-9)

where

- K = loss coefficient;
- $A_K$  = area associated with the loss coefficient (not necessarily equal to the flow area);
- $\rho_\ell$  = liquid density at the restriction (In subcooled flow,  $\rho_\ell$  is linearly interpolated to the elevation of the flow restriction; in two-phase flow,  $\rho_\ell$  is saturated liquid density); and
- $\phi_{TPL}^2$  = two-phase local loss multiplier.

(4-10)

The final pressure drop component in Equation 4-1 results from acceleration. This includes the reversible pressure difference experienced by a fluid at an area change (the irreversible component is accounted for with a local loss coefficient) and the pressure difference resulting from density changes such as steam formation.

The reversible pressure difference resulting from a flow area change is given by:

(4-11)

where

$$\sigma_A = \frac{A_2}{A_1} = \frac{\text{final flow area}}{\text{initial flow area}}$$

The density  $\rho$  in Equation 4-11 is generated differently for single-phase and two-phase flow. In single-phase flow,  $\rho$  is the fluid density of the sub-cooled liquid at the elevation of the area change. In two-phase flow:

$$\rho = \frac{\rho_{KE}^2}{\rho_H} \quad (4-12)$$

where

$\rho_{KE}$  = kinetic energy density, and

$\rho_H$  = homogeneous density.

The kinetic energy density is defined by:

$$\frac{1}{\rho_{KE}^2} = \frac{X^3}{\left(\rho_g \alpha\right)^2} + \frac{(1-X)^3}{\left[\rho_f (1-\alpha)\right]^2} \quad (4-13)$$

and the homogeneous density is given by:

$$\frac{1}{\rho_H} = \frac{X}{\rho_g} + \frac{(1-X)}{\rho_f} \quad (4-14)$$

The acceleration pressure difference due to a density change is given by:

$$\Delta P_{acc} = \frac{1}{g_c} \left(\frac{W}{A}\right)^2 \left[ \frac{1}{\rho_{H_2}} - \frac{1}{\rho_{H_1}} \right] \quad (4-15)$$

where  $\rho_H$  is the homogeneous water density.

An iterative process is required to determine the flow in each characteristic channel which results in equal channel pressure drop for all channels while preserving total core flow. The characteristic channel flow rates are then distributed to individual channels of the same geometry and orifice type by linear interpolation on total channel power, axial power shape, and crud thickness.

#### 4.2 ENTHALPY-QUALITY DISTRIBUTION CALCULATION

Once the flow into each channel has been determined, an energy balance up the channel is used to calculate enthalpy at each axial node. (See Figure A-1 in Appendix A for axial nodalization.) Quality is directly related to enthalpy. Similar calculations were required for each characteristic channel during the determination of flow distribution.

Figure 4-2 illustrates the geometry of a typical flow channel. The nodal energy balance for in-channel coolant flow accounts for the following components:

- (1) energy carried by coolant from the node below;
- (2) energy deposited in the coolant by heat flux through the fuel rod cladding;
- (3) energy absorbed by the coolant from neutron slowing down and gamma heating;
- (4) energy absorbed by the channel wall from neutron slowing down and gamma heating which is transferred to the coolant by conduction and convection; and
- (5) energy transferred by convection and conduction from in-channel coolant to bypass coolant through the channel wall.

The core inlet enthalpy (subcooling) is a given quantity. Neutron slowing-down and gamma heating factors are obtained from detailed X-Y physics calculations performed for lattice cells parametrically as a function of coolant density, control rod position (in or out), and lattice geometry.

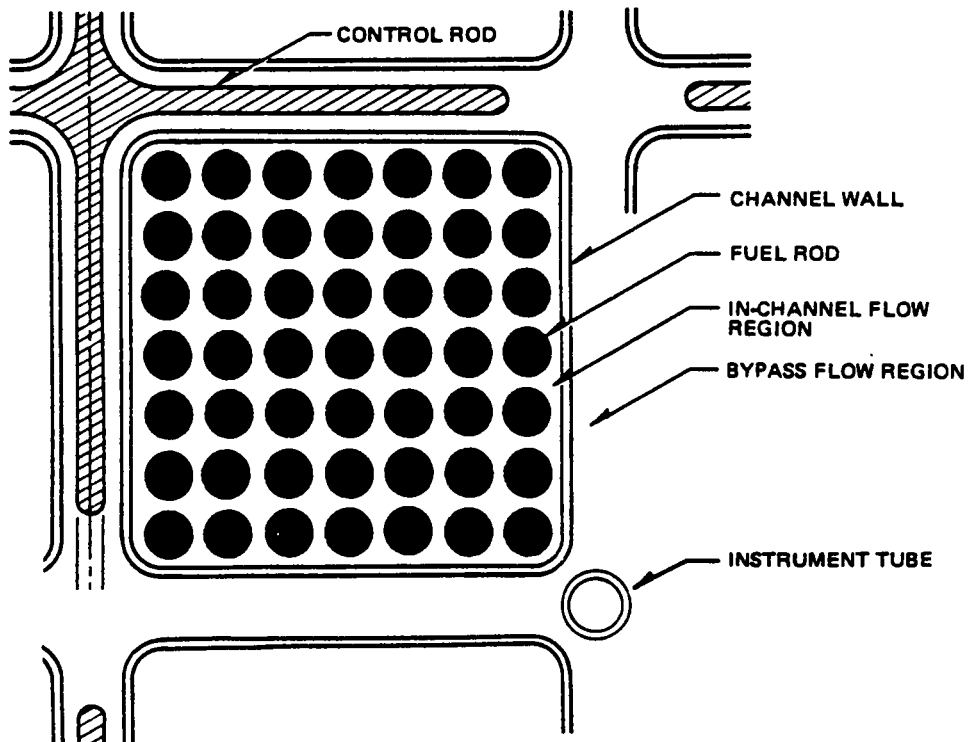


Figure 4-2. Flow Channel Geometry

The in-channel coolant energy and mass flows yield enthalpy  $h$  at axial level  $k$ . Flow quality at level  $k$  is given by:

$$X = \frac{h - h_{\ell}}{h_g - h_{\ell}} \quad (4-16)$$

where  $h_g$  is saturated vapor enthalpy and  $h_{\ell}$  is bulk liquid enthalpy. The bulk liquid enthalpy calculation accounts for subcooled boiling effects and the bulk boiling limit, where  $h_{\ell}$  is simply the saturated liquid enthalpy  $h_f$ . Vapor flow (boiling) is indicated whenever  $X > 0$ .

#### 4.3 VOID-QUALITY CORRELATION

A modified Zuber-Findlay correlation similar to that described in Reference 4-2 is used to convert flow quality to void fraction at each level  $k$ . This void-quality correlation provides a physically oriented representation of subcooled, intermediate, and bulk boiling through empirical constants appearing in the concentration parameter  $C_o$  and the drift velocity term  $V_{gj}$ . The former represents the detailed distribution of vapor and liquid in the flow cross-sectional area; the latter describes the drift of vapor bubbles relative to bulk coolant flow. The correlation is:

$$(4-17)$$

where  $\alpha_H$  is the homogeneous flow void fraction.  $C_o$  and  $V_{gj}$  are represented by correlations based on coolant properties and are locally linear in the void fraction  $\alpha$ . Therefore, a quadratic equation must be solved in order to determine  $\alpha$ . Separate correlations are used for  $V_{gj}$  in the Bubbly-Churn-Turbulent, Transition, and Annular regions.

Data used to determine the empirical constants in  $C_o$  and  $V_{gj}$  were obtained from single and multirod assembly void measurements. The relative moderator density given by Equation 2-22 represents void feedback coupling between the thermal-hydraulics model and the nuclear model.

#### 4.4 BYPASS REGION CALCULATION

Thermal-hydraulics effects in the bypass flow region are modeled in a manner similar to the in-channel flow region. The following assumptions are used:

- (1) Coolant mixes uniformly in the bypass region; therefore, only one bypass flow region is considered. That is, the gaps between all fuel bundles (Figure 4-2) are lumped together to form one uniform flow region.
- (2) Inlet flow and enthalpy to the bypass region are given.
- (3) The average control rod fraction at level  $k$  is used to determine the bypass flow area and heating resulting from  $\gamma$ ,  $(n,\gamma)$ , and  $(n,\alpha)$  reactions in the control rods.
- (4) The temperature of water in the vessel annulus (downcomer) region is equal to the core inlet temperature.

As for in-channel coolant flow, a nodal energy balance is performed for the bypass coolant. The following components are considered:

- (1) energy carried by coolant from the node below;
- (2) energy absorbed by the coolant from neutron slowing down and gamma heating;
- (3) energy absorbed by the channel wall from neutron slowing down and gamma heating which is transferred to the coolant by conduction and convection;
- (4) energy transferred by convection and conduction from in-channel coolant to bypass coolant through the channel wall;

- (5) energy absorbed by control rods from  $\gamma$ ,  $(n,\gamma)$  and  $(n,\alpha)$  reactions which is transferred to the coolant by conduction and convection; and
- (6) energy transferred by convection and conduction from bypass coolant to water in the vessel annulus through the core shroud.

The energy contribution from heat generation in the core shroud and upper and lower core structures is ignored. This is compensated by neglecting energy losses due to neutron and gamma leakage from the core.

Once energy to the bypass coolant is determined, axial enthalpy, flow quality, and void distributions are calculated following the same procedure used for in-channel flow.

#### 4.5 TOTAL CORE ENERGY BALANCE

When performing a BWR simulation, the total core power level is given. It is necessary to insure that the power absorbed by in-channel coolant and bypass coolant sums to the given total core power level.

Specifically, the neutron and gamma direct heating components of the nodal energy balances are expressed in terms of fuel rod heat flux through the cladding for each channel. For example, energy absorbed by the channel wall from neutron slowing down and gamma heating is given by the ratio of direct heating in the channel wall relative to cladding heat flux. Therefore, each direct heating component of the nodal energy balance is written as the product of cladding heat flux times the appropriate direct heating ratio. The cladding heat flux (more than 95% of the total core power) becomes a parameter which may be adjusted until the power deposited into the coolant equals the given total core power level. This adjustment is performed during the outer loop of the power-void iteration (Figure 2-1).

(4-18)

where  $n$  represents each flow channel,  $b$  represents the bypass region,  $h_i$  and  $h_e$  are inlet and exit enthalpy, respectively. The average cladding heat flux at node  $(i,j,k)$  is:

$$\bar{Q}_{i,j,k} = P_{i,j,k} P_C F_Q / S_{i,j} \quad (4-19)$$

$P_{i,j,k}$  = power distribution (normalized to 1.0)

$F_Q$  = fraction of total power per channel which is transmitted by convection from fuel rod cladding to in-channel coolant

$S_{i,j}$  = cladding heat transfer surface area for the channel at  $(i,j)$

$F_Q$  is the parameter that is adjusted each power-void iteration until  $P_C$  is equal to the given total core power level.

#### 4.6 THERMAL LIMITS CALCULATION

Once the power-void iteration is converged, the nodal power distribution is in equilibrium with the distribution of feedback effects (moderator density, fuel temperature, xenon poisoning, and crud deposition). Detailed core performance characteristics may then be determined. Three important characteristics with respect to thermal performance limits are: (1) peak cladding heat flux (Btu/h-ft<sup>2</sup>); (2) maximum and average fuel rod linear heat generation rate (kW/ft); and (3) critical power ratio. The latter quantity (CPR) expresses margin relative to boiling transition.

The nuclear model determines average power for each  $(i,j,k)$  node by Equation 2-38. For thermal limits evaluation, it is necessary to calculate the peak power within the node (i.e., the maximum fuel rod power within the bundle represented by the node). A correlation is used to relate peak rod power to average bundle power; this ratio is called local peaking factor. The

correlation is expressed in terms of U, UH, E, and control for each fuel type. Local peaking factor data are obtained from the same detailed lattice physics calculations which produce the other parameters used in the nuclear model.

Peak cladding heat flux at node (i,j,k) is:

$$\hat{Q}_{i,j,k} = (F_L \bar{Q})_{i,j,k} \quad (4-20)$$

where  $F_L$  represents local peaking factor. The maximum and average fuel rod linear heat generation rates are:

$$\widehat{LHGR}_{i,j,k} = \hat{Q}_{i,j,k} O_{i,j} \quad (4-21)$$

and

$$\overline{LHGR}_{i,j,k} = \bar{Q}_{i,j,k} O_{i,j} \quad (4-22)$$

where  $O_{i,j}$  is the heated perimeter per fuel rod for the channel at (i,j). It is assumed that each fuel rod in the bundle has the same  $O$ . Note that  $\overline{LHGR}$  given by Equation 4-22 is normally referred to as average planar linear heat generation rate (APLHGR).

The GE Thermal Analysis Basis (GETAB) (Reference 4-3) is used to identify thermal margin relative to boiling transition. The GEXL correlation predicts bundle average critical quality  $X_C$  by the general form:

(4-23)

For each channel type, R is dependent upon channel average exposure and control configuration. Local peaking pattern data for R are obtained from the detailed lattice physics calculations. Critical power ratio (CPR) is defined as the ratio of bundle power which would yield  $X_C$  (boiling transition) relative to existing bundle power. As used here, the term bundle power is the total power absorbed by in-channel coolant for a particular channel.

#### 4.7 REFERENCES

- 4-1. C.A. Meyer et. al., "Thermodynamic and Transport Properties of Steam," American Society of Mechanical Engineers (1967).
- 4-2. G.E. Dix, "Vapor Void Fractions for Forced Convection with Subcooled Boiling at Low Flow Rates", NEDO-10491, January 1973.
- 4-3. "General Electric BWR Thermal Analysis Basis (GETAB): Data, Correlation and Design Application", NEDO-10958, November 1973.

## 5. MODEL QUALIFICATION

### 5.1 INTRODUCTION

The models in this report have been qualified against data obtained from operating Boiling Water Reactors. The qualification studies consist of:

- (1) simulation and tracking of nine operating cycles on three plants;
- (2) three-dimensional global power distribution comparisons with gamma scan measurements taken at the end of six cycles; and (3) cold critical measurements taken at the end of six cycles; (3) cold critical measurements taken during seven cycles and two plants; and (4) burnup verification data at the end of one cycle.

### 5.2 PLANT TRACKING RESULTS

In plant tracking calculations, the 3-D simulator (using cross sections generated from the lattice model) is used to simulate the behavior of a plant during operation. The reactor power, flow and pressure are input to the simulator, which then calculates the core  $k_{\text{eff}}$  and power distributions as a function of cycle exposure. The operating reactor is critical; hence, the calculated  $k_{\text{eff}}$  is compared to 1.0. Accurate and technically well-founded simulators should calculate a  $k_{\text{eff}}$  close to 1.0 and the difference between  $k_{\text{eff}}$  and 1.0 should not vary appreciably from plant to plant or as a function of fuel exposure. Consistency of  $k_{\text{eff}}$  bias ensures that accurate cycle length estimates will be obtained in future core designs. Figures 5-1 through 5-9 show plots of calculated  $k_{\text{eff}}$  as a function of cycle exposure for Hatch 1 (Cycles 1 through 3), Quad Cities 1 (Cycles 1 through 5), and Millstone 1 (Cycle 7) (References 5-1 through 5-8). The average and the RMS deviation of  $k_{\text{eff}}$  for each cycle are summarized in Table 5-1. The overall average is 1.002 with an RMS of 0.002, which is a quite narrow band considering the data are compiled over three plants and over nine cycles.

Figures 5-10 through 5-18 compare computed and measured axial power shapes at beginning and end of cycle for each of the nine cycles above. These figures show the 3-D simulator to give an accurate estimate of average axial power.

Table 5-1  
SUMMARY OF HOT CRITICAL  $k_{eff}$

Figure 5-2. Hatch 1 Cycle 2:  $k_{eff}$  Versus Exposure

Figure 5-3. Hatch 1 Cycle 3:  $k_{eff}$  Versus Exposure

Figure 5-4. Quad Cities 1 Cycle 1:  $k_{eff}$  Versus Exposure

CYCLE EXPOSURE (GWd/t)

Figure 5-5. Quad Cities 1 Cycle 2:  $k_{eff}$  Versus Exposure

Figure 5-6. Quad Cities 1 Cycle 3:  $k_{eff}$  Versus Exposure

Figure 5-7. Quad Cities 1 Cycle 4:  $k_{eff}$  Versus Exposure

Figure 5-8. Quad Cities 1 Cycle 5:  $k_{eff}$  Versus Exposure

Figure 5-9. Millstone Cycle 7:  $k_{eff}$  Versus Exposure

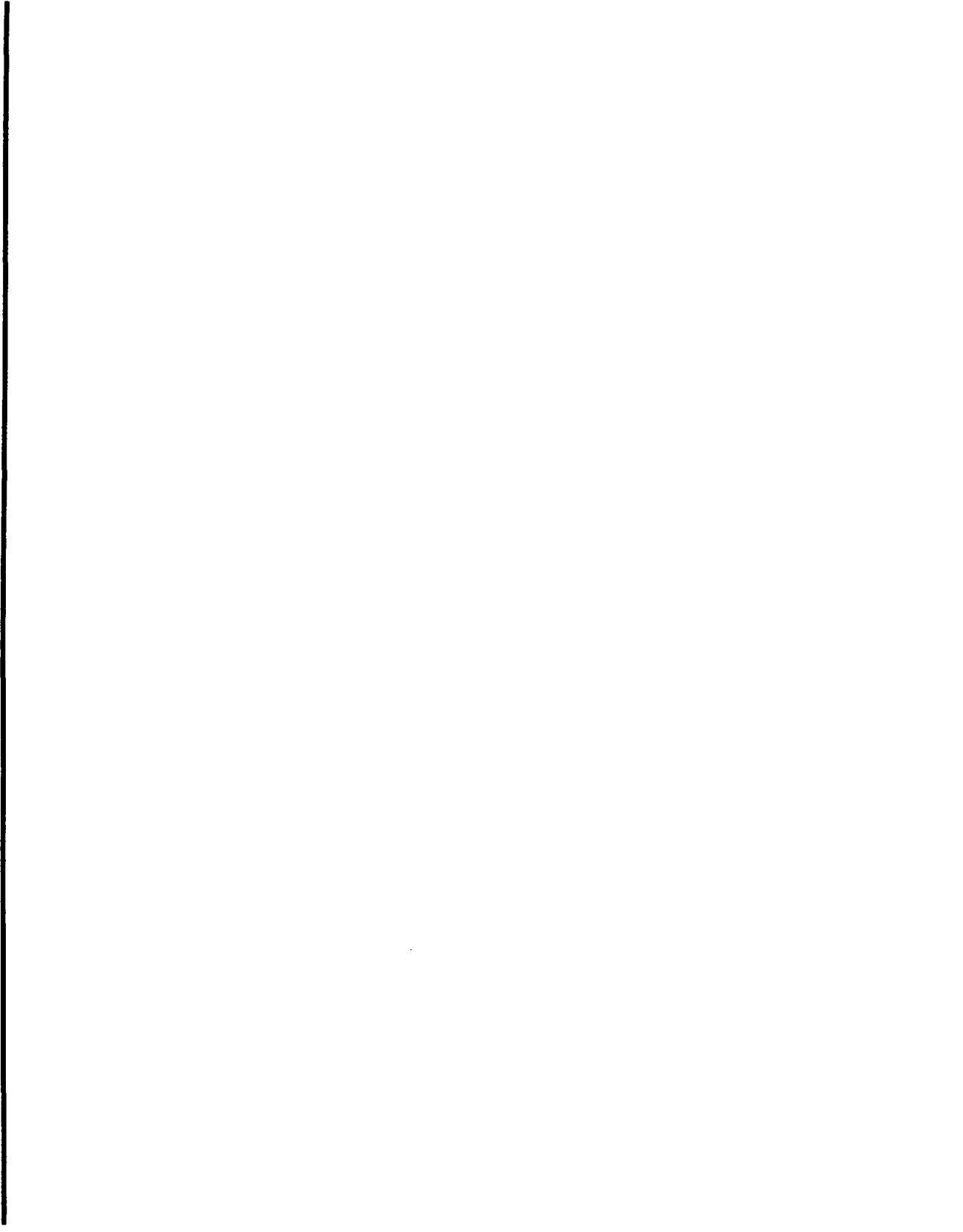


Figure 5-10. Hatch 1 Cycle 1: Core Average Axial Power

Figure 5-11. Hatch 1 Cycle 2: Core Average Axial Power

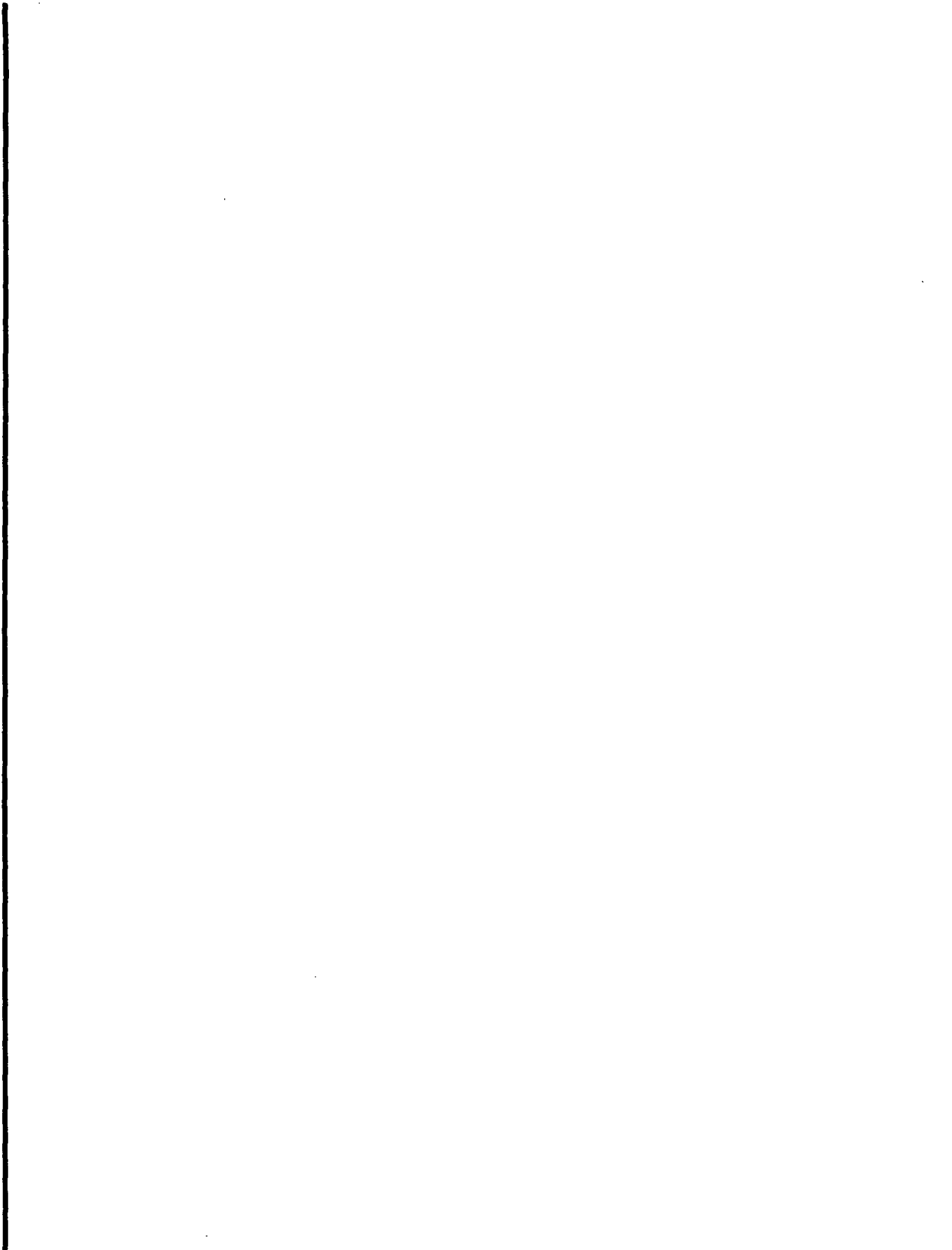


Figure 5-12. Hatch 1 Cycle 3: Core Average Axial Power

Figure 5-13. Quad Cities 1 Cycle 1: Core Average Axial Power



Figure 5-14. Quad Cities 1 Cycle 2: Core Average Axial Power

Figure 5-15. Quad Cities 1 Cycle 3: Core Average Axial Power



Figure 5-16. Quad Cities 1 Cycle 4: Core Average Axial Power

Figure 5-17. Quad Cities 1 Cycle 5: Core Average Axial Power

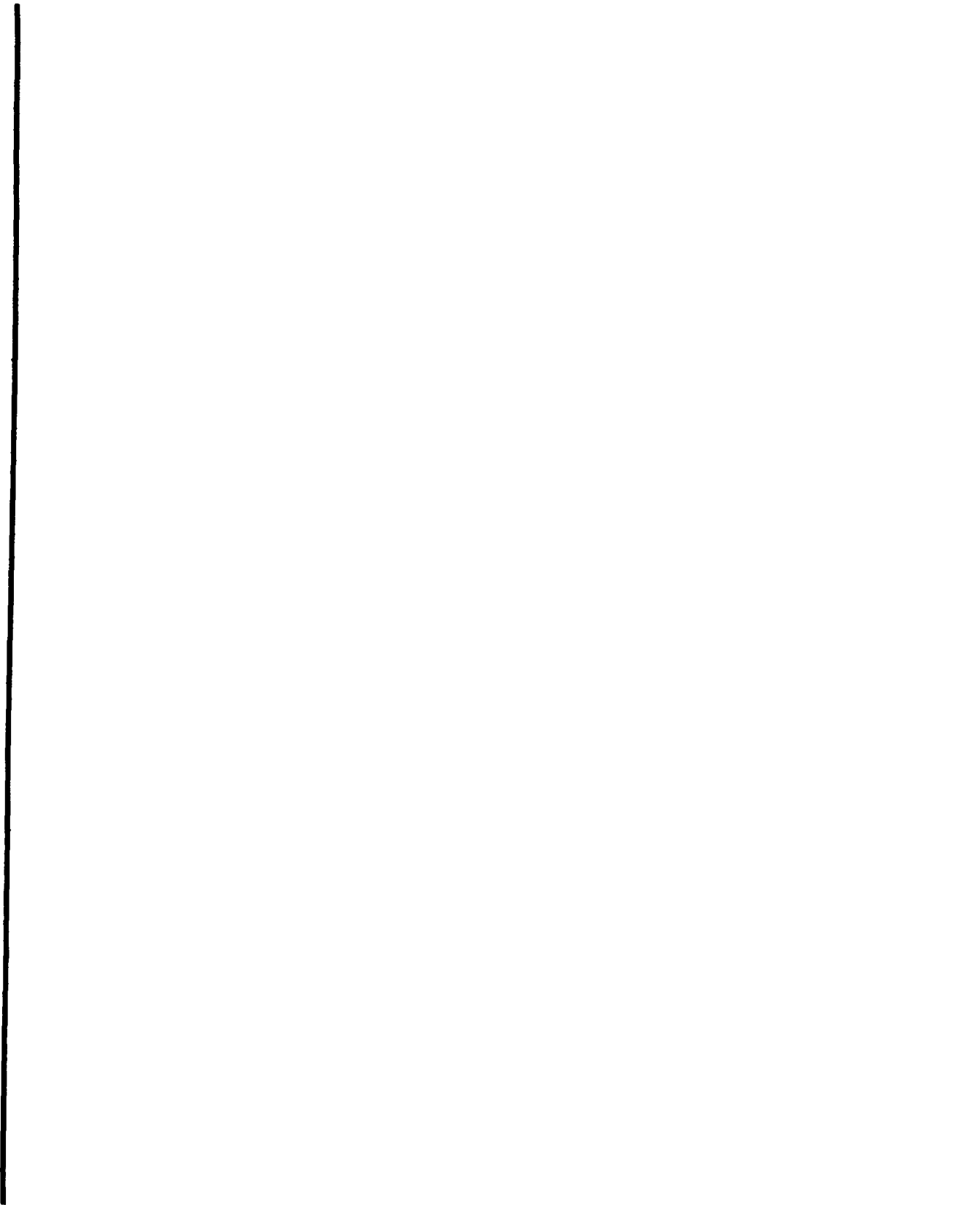


Figure 5-18. Millstone 1 Cycle 7: Core Average Axial Power

## 5.2 GAMMA SCAN COMPARISONS

Traversing in-core probe (TIP) signals are used, together with the process computer, to monitor the three-dimensional power distribution in the reactor during operation. The TIP signals provide a good picture of the axial power distribution but do not provide a detailed bundle by bundle distribution because there is only 1 TIP location for every 16 bundles. A more accurate estimate of the reactor power distribution can be obtained just prior to a reactor shutdown by the procedure known as gamma scanning (References 5-1, 5-4, 5-5 and 5-8). The gamma scan technique consists of removing the fuel bundles from the reactor core and measuring the gamma ray intensity as a function of axial position in the bundle. The gamma ray measured is the 1596 KeV gamma ray coming from Lanthinum-140.

The Lanthinum-140 comes from the beta decay of Barium-140, a fission product with a half-life of 12.79 days. Measurement of the Lanthinum-140 activity and correction for the Barium-140 decay yields a relative Barium-140 concentration as a function of position in the core just prior to shutdown. The Barium-140 distribution, in turn, closely follows the actual power distribution.

Global gamma scan measurements have been performed at the end of six cycles: Cycles 1 and 3 of Hatch 1; Cycles 2, 4, and 5 of Quad Cities 1; and Cycle 7 of Millstone 1. In each of the cases, roughly one-eighth of the bundles in the octant symmetric core were scanned. The relative concentration of Barium-140 has been calculated by the 3-D simulator using the plant tracking calculations described in Section 5.1, using the power distributions calculated near the end of cycle coupled with the Barium-140 decay equations. Figures 5-19 through 5-24 compare the calculated and measured axial Barium-140 distribution for the six global gamma scan measurements. In each case the agreement is quite good. Figures 5-25 through 5-30 show the percent error in bundle integrated power as a function of position in the core octant. In the interior of the core the agreement in bundle average power is quite good. The percent errors are somewhat larger near the edge of the core, where the power density is low. The overall nodal and bundle RMS differences are summarized in

Table 5-2.  
NODAL AND BUNDLE INTEGRATED POWER COMPARISONS  
GAMMA SCAN VS. CALCULATION

$$*_{\text{RMS}} \equiv \frac{1}{N-1} \left( \sum_{i=1}^N (P_i^{\text{calculated}} - P_i^{\text{measured}})^2 \right)^{1/2}$$

$P_i$  = nodal or bundle power density

Figure 5-19. Hatch 1, Cycle 1: Axial  
Barium Distribution

Figure 5-21. Quad Cities 1, Cycle 2: Axial  
Barium Distribution

Figure 5-20. Hatch 1, Cycle 3: Axial  
Barium Distribution

Figure 5-22. Quad Cities 1, Cycle 4: Axial  
Barium Distribution

---

Figure 5-23. Quad Cities, Cycle 5: Axial Barium Distribution

Figure 5-24. Millstone, Cycle 7: Axial Barium Distribution

Figure 5-25. Hatch 1, End of Cycle 1: Bundle Power Comparisons



Figure 5-26. Hatch 1, End of Cycle 3: Bundle Power Comparisons

Figure 5-27. Quad Cities 1, End of Cycle 2: Bundle Power Comparisons



Figure 5-28. Quad Cities 1, End of Cycle 4: Bundle Power Comparisons

Figure 5-29. Quad Cities 1, End of Cycle 5: Bundle Power Comparisons



Figure 5-30. Millstone End of Cycle 7: Bundle Power Comparisons

Table 5-2. The nodal RMS varies between 4% and 6% and the integrated bundle RMS varies between 2% and 3%.

### 5.3 COLD CRITICAL MEASUREMENTS

BWRs are designed so that they can be shut down in the cold condition (68°F) with a single control blade withdrawn. In order to qualify the ability of the 3-D simulator to accurately predict the cold shutdown margin, a number of cold critical experiments have been performed. In all cases, enough control blades were withdrawn to make the reactor critical. In some selected experiments, special blade patterns were used to simulate single withdrawn control blade configuration. Those critical experiments carried out at Hatch 1 during Cycles 1 through 3 and Quad Cities 1 during Cycles 1 through 4 have been analyzed. The results of the cold critical experiments are summarized in Table 5-3. The average cold calculated  $k_{eff}$  is 0.9986 with an overall standard deviation of 0.0033. All cold shutdown calculations used in design analysis are biased with results obtained through the analysis of cold critical experiments. The overall standard deviation is a measure of the uncertainty in this bias.

### 5.4 ISOTOPIC BURNUP VERIFICATION

Table 5-3  
 QUAD CITIES COLD CRITICAL EIGENVALUES

<u>Cycle</u>	<u>Total Notches</u>	<u>Cycle Exposure (MWd/ST)</u>	<u>Calculated <math>k_{eff}</math></u>
1	6384	0.0	1.0052
	6758	2474	0.9976
	7166	3480	0.9941
	6418	6175	0.9972
2	6224	953	0.9957
	5928	1683	0.9942
	5600	3059	0.9923
3	8422	0.0	1.0001
	8382	0.0	0.9953
	8404	0.0	0.9981
4	6462	0.0	1.0026
	6408	1200	1.0010

HATCH-1 COLD CRITICAL EIGENVALUES

<u>Cycle</u>	<u>Total Notches</u>	<u>Cycle Exposure (MWd/ST)</u>	<u>Calculated <math>k_{eff}</math></u>
1	6378	0.0	1.0022
	4786	0.0	1.0014
	4738	0.0	1.0003
	4642	375	1.0016
	4730	1086	1.0000

Table 5-3 (Continued)

<u>Cycle</u>	<u>Total Notches</u>	<u>Cycle Exposure (MWd/ST)</u>	<u>Calculated <math>k_{eff}</math></u>
2	4932	0.0	0.9973
	5170	2308	0.9957
	4788	3129	0.9973
3	4832	0.0	<u>1.0016</u>
Average			0.9986
Standard Deviation			0.0033



Figure 5-31. Quad Cities-1 Core Loading, Cycle 2

Figure 5-32. MO<sub>2</sub> Bundle, Center Design



Table 5-4  
MEASURED EXPOSURES (MWD/ST)

Figure 5-33. Void Fraction History of Central MO<sub>2</sub> Bundle GEB161

Figure 5-34. Power Density History of Central MO<sub>2</sub> Bundle GEB161

---

---

Table 5-5  
SUMMARY OF AVERAGE PERCENT ERRORS

Table 5-6  
NUCLIDE DENSITY COMPARISON FOR U235/U



---

Table 5-7  
NUCLIDE DENSITY COMPARISON FOR U236/U

Table 5-8  
NUCLIDE DENSITY COMPARISON FOR U238/U



---

Table 5-9  
NUCLIDE DENSITY COMPARISON FOR PU/U

Table 5-10  
NUCLIDE DENSITY COMPARISON FOR PU239/PU

---

Table 5-11  
NUCLIDE DENSITY COMPARISON FOR PU240/PU

Table 5-12  
NUCLIDE DENSITY COMPARISON FOR PU241/PU

---

Table 5-13  
NUCLIDE DENSITY COMPARISON FOR PU242/PU

Table 5-14  
NUCLIDE DENSITY COMPARISON FOR U236/U235

5-45

NEEDO-30130-A



---

Table 5-15  
NUCLIDE DENSITY COMPARISON FOR PU239/U238

Table 5-16  
NUCLIDE DENSITY COMPARISON FOR PU240/PU239

5-47

NEEDO-30130-A

---

---

Table 5-17

NUCLIDE DENSITY COMPARISON FOR PU241/PU240

Table 5-18  
NUCLIDE DENSITY COMPARISON FOR PU242/PU241

## 5.5 REFERENCES

- 5-1. L.M. Shiraishi and G.R. Parkos, "Gamma Scan Measurements at Edwin I. Hatch Nuclear Plant Unit 1 Following Cycle 1," EPRI NP-511, 1978.
- 5-2. N.H. Larsen and J.L. Goudy, "Core Design and Operating Data for Cycle 1 of Hatch 1," EPRI NP-562, 1979.
- 5-3. G.L. Holloway, "Core Design and Operating Data for Cycles 2 and 3 of Hatch 1," EPRI NP-2106, October 1981.
- 5-4. H.D. Kosanke, M.C. Gregory, J.T. Ma, and B.W. Crawford, "Gamma Scan Measurements at Edwin I. Hatch Nuclear Plant Unit 1 Following Cycle 3," EPRI NP-2105, December 1981.
- 5-5. M.B. Cutrone and G.F. Valby, "Gamma Scan Measurements at Quad Cities Nuclear Power Station Unit 1 Following Cycle 2," EPRI NP-214, July 1976.
- 5-6. N.H. Larsen "Core Design and Operating Data for Quad Cities 1 Cycle 3," EPRI NP-552, March 1983.
- 5-7. M.R. Alkowni and J.T. Ma, "Core Design and Operating Data for Quad Cities 1 Cycle 4," NEDC-25490, November 1981.

- 5-8. H.D. Kosanke, "Gamma Scan Measurements at Quad Cities 1 Following Cycle 4," NEDC-25492, November 1981.
- 5-9. R.M. Tilley et al., "Burnup and Transuranium Element Composition in Irradiated  $UO_2$ ,  $UO_2-Gd_2O_3$ , and  $UO_2-PuO_2$  Rods from the Quad Cities-1 Reactor," EPRI NP-2307-LD (March 1982).



APPENDIX A  
CORE GEOMETRY FOR NUCLEAR MODEL

The core is described in X-Y-Z geometry with the restriction that there is equal mesh spacing in the X-Y directions. The X, Y, Z mesh is indicated by i, j, k nomenclature, respectively (Figures A-1 and A-2). In a horizontal plane, each fuel assembly or flow channel is described by one mesh point at the center. Mesh point (1,1,k) is in the upper left corner of horizontal plane, k. Vertically, the first point (k=1) is ( $\Delta Z/2$ ) away from the bottom, and the last point (k=KMAX) is ( $\Delta Z/2$ ) from the top. The program is presently dimensioned for a maximum of 34x34 bundles and 50 axial planes, or 57,800 mesh points. In addition to full core representation, quarter-core and half-core options are available with either mirror or rotational symmetry conditions (Figure A-2).

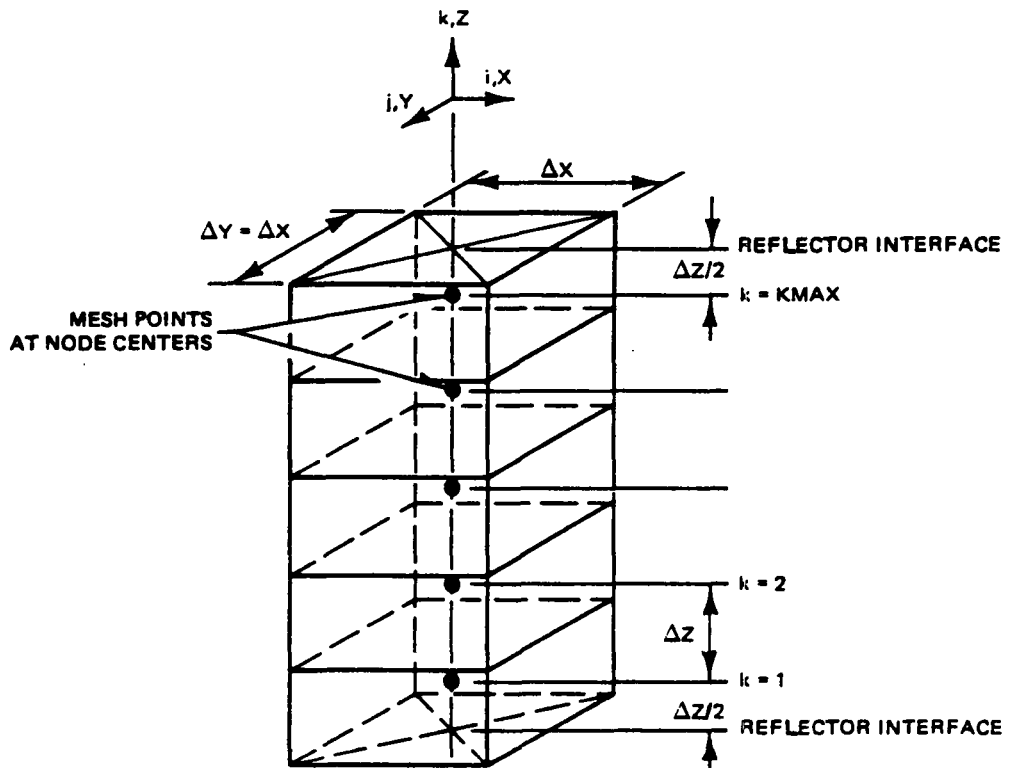


Figure A-1. Node and Mesh Arrangement for a Given Channel

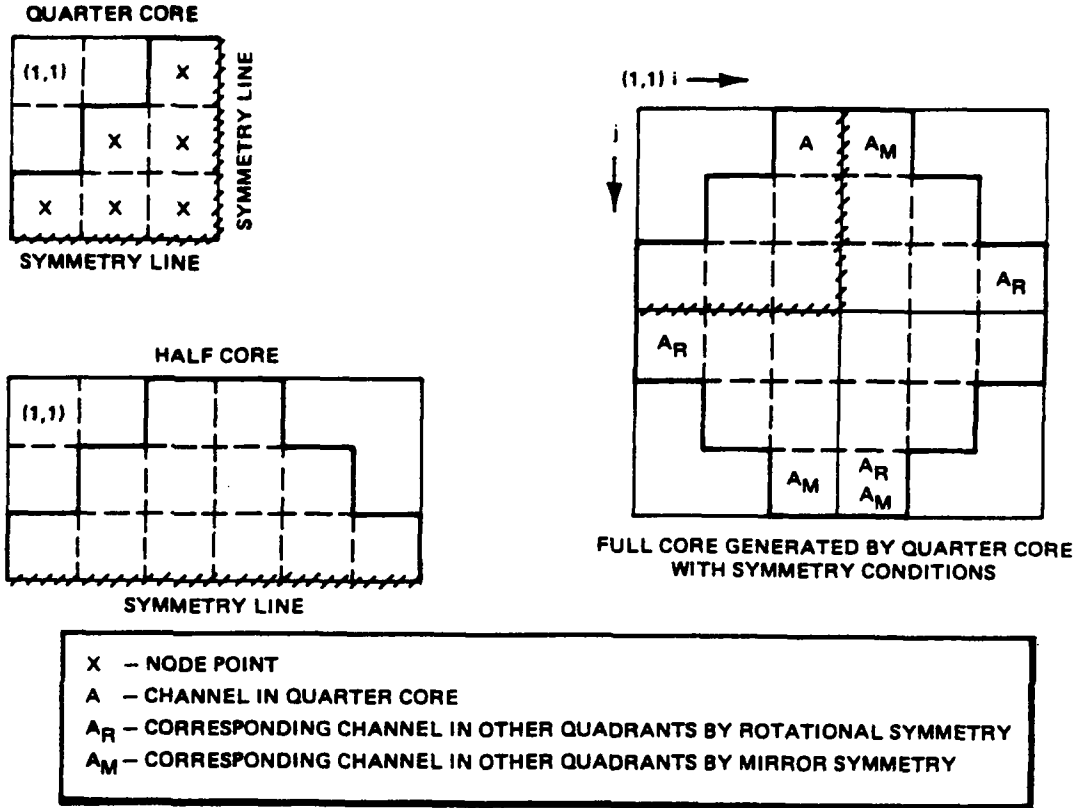


Figure A-2. BWR Symmetry Options

A.1 CHANNEL TYPES

Different fuel assembly characteristics are provided by making the appropriate quantities channel-type-dependent (it-dependent). The channel types are defined by the  $IAT_{i,j}$  input array. Non-zero entries in this array define a fuel assembly of type  $it$  at the location  $(i,j)$  in the core. All mesh points in a vertical mesh line have the same channel type characteristics (Figure A-3).

The thermal-hydraulic and geometric properties of a fuel assembly are channel-type-dependent. Different channel types are channels with different flow properties, axial Gd distribution, channel thickness, fuel rod diameter, flow area, etc. A typical plant might have three channel types for the initial loading with different axial Gd distributions. Subsequent core loadings could have more channel types. The program presently is dimensioned for a maximum of 20 channel types.

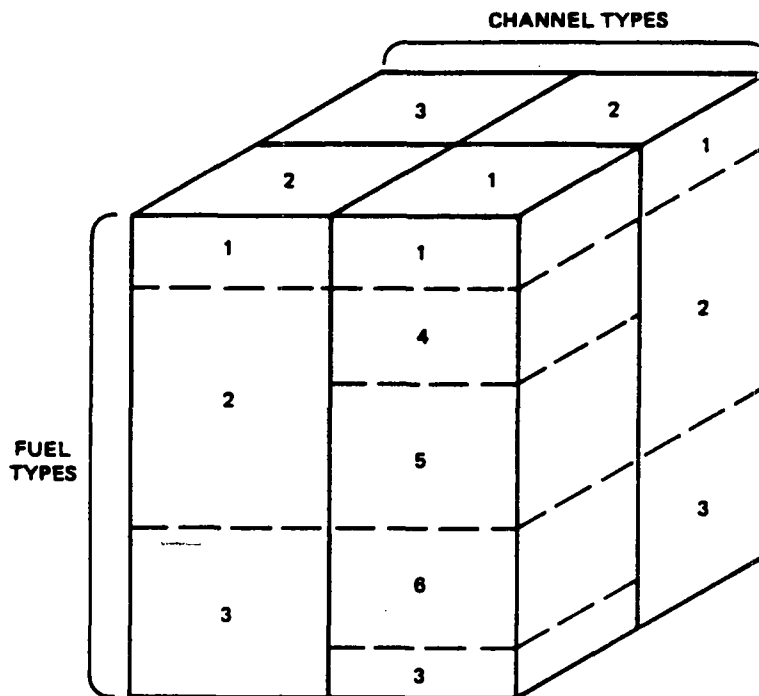


Figure A-3. Channel and Fuel Types

## A.2 FUEL TYPES

Different fuel characteristics are provided by definition of a fuel type,  $it$ , which may vary axially within each channel type. The fuel types are input of the  $IFT_{k,it}$  array. This two-dimensional array defines the fuel type present at axial node  $k$  in channel type  $it$ . Thus, all channels of type  $it$  have the same axial fuel characteristics (Figure A-3).

The nuclear properties within individual planes of a fuel assembly vary with fuel type. Different fuel types typically are defined for varying initial enrichments, gadolinia poison rods, etc. The program is presently dimensioned for a maximum of 20 fuel types.

## A.3 ORIFICE TYPES

Any of three different orifice types can be associated with the location  $(i,j)$  by the  $IORF_{i,j}$  input array. The channel flow and bypass flow correlation coefficients are a function of  $IORF_{i,j}$ . The orifice type is set and, even though the fuel at  $(i,j)$  is moved to  $(i',j')$ , the orifice type remains at  $(i,j)$ . This allows an analysis of both a fixed grid plate orificing

arrangement and channels in which the orificing is built into the nose piece of the fuel assembly, since orifice loss coefficients can also be assigned to the channel itself.

A.4 CONTROL ROD POSITIONS

A control rod may be associated with each channel in the core. The control rod for point (i,j,k) is located in the lower right corner of the channel at (i,j) (Figure A-4). The input magnitude of  $ROD_{i,j}$  is the number of mesh intervals that the control rod associated with channel (i,j) is withdrawn.

A.5 IN-CORE MONITOR POSITIONS

Similar to the control rod definition, the in-core monitor and traveling in-core probe (TIP) locations are assigned to the lower right of a mesh point (Figure A-4). The location of the monitors is only needed for an edit of

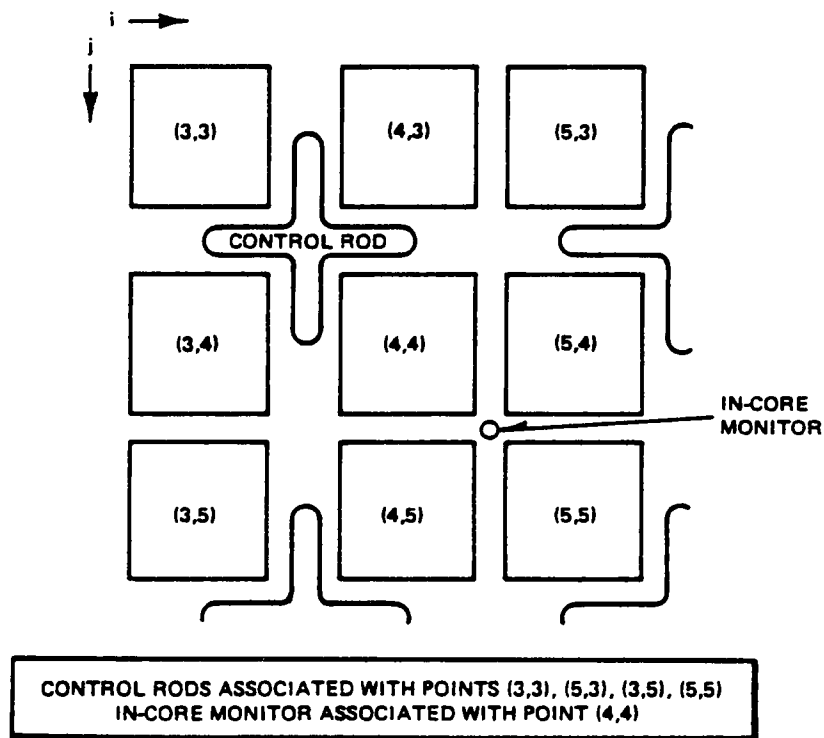


Figure A-4. Control Rod and Monitor Positions

simulated instrument response. This is specified by inputting one (1) in the appropriate locations of the input  $TIP_{i,j}$  array. TIP or chamber response is edited for each k point in the lower right corner of every i,j location where  $TIP_{i,j}$  is non-zero.

